Precambrian Research 393 (2023) 107091

Contents lists available at ScienceDirect

Precambrian Research

journal homepage: www.elsevier.com/locate/precamres

Co-existing two distinct formation mechanisms of micro-scale ooid-like manganese carbonates hosted in Cryogenian organic-rich black shales in South China

Jiayi Ai [a,b], Sandra Siljeström [c], Ningning Zhong [a,*], Jianfa Chen [a], Tieguan Wang [a], Nansheng Qiu [a], Simon C. George [b]

[a] State Key Laboratory of Petroleum Resources and Prospecting, College of Geosciences, China University of Petroleum (Beijing), Beijing 102249, China
[b] School of Natural Sciences, Macquarie University, Sydney, NSW 2109, Australia
[c] RISE Research Institutes of Sweden, 11486 Stockholm, Sweden

ARTICLE INFO

Keywords:
Manganese deposit
Black shale
Microbial mediation
Physiochemical pathway
Cryogenian
Carbon cycle

ABSTRACT

Manganese-rich deposits in the lower member of the Datangpo Formation (DTP) (ca. 663–654 Ma) in South China formed in the aftermath of the Cryogenian Sturtian glaciation. The Mn in the DTP occurs dominantly as rhodochrosite and Ca-rhodochrosite. A hydrothermal origin of the Mn^{2+} is shown by the rare earth element distribution and significantly high Mn/Fe ratios (3–19, average = 10.1). Previous studies suggested a microbially-mediated process for controlling the DTP black-shale hosted Mn carbonate deposits. However, detailed reports on the formation mechanisms of micro-scale (<2–5 μm) ooid-like Mn carbonates in the DTP have rarely been published. Systematic petrography and geochemical analyses in this study demonstrate the coexistence of two types of micro-scale ooidal-like Mn carbonates formed through two distinct mechanisms, either dominated by microbially-mediated or physiochemically-forced pathways. The Type I Mn carbonate has relatively larger grain size of 2–5 μm and exhibits a radial-concentric microfabric that shows signs of growth banding in the form of alternating light and dark laminae, which mainly express variation in Ca and Mn concentrations. The initial precipitation phase of the Type I Mn carbonate is interpreted to be Mn oxide/hydroxide, based on positive Ce anomalies and selective enrichments of particular trace elements. Novel evidence indicates that the capture of Mn as a carbonate phase directly from the water column by primarily precipitated calcite, which is referred to as the Type II Mn carbonate, has also contributed to the DTP Mn-rich deposits. Multiple roles of organic matter in Mn carbonate formation have been established: (1) catalysed Mn-redox cycling; (2) trapping and transportation of initial mineral precipitates to sediments; (3) serving as a carbon source; (4) regulating the morphology of the Mn carbonate. As a key link for understanding Cryogenian carbon and Mn cycling, specific formation pathways for the DTP Mn-carbonates are likely to have been controlled by given atmospheric-oceanic compositions (including oxygen level, pCO_2, and redox conditions) in response to major geological and biological events during the interglacial period. In turn, massive storage of inorganic carbon and phosphorous in Mn carbonate phases would have had a substantial influence on biogeochemical carbon cycling during the Cryogenian.

1. Introduction

Major changes in Earth's exogenic environments through geological history, such as extreme climate variation (i.e., Snowball Earth and Greenhouse episodes), are dynamically guided by tectonic movements, including the assembly and breakup of supercontinents, which are orchestrated by mantle perturbations (Condie et al., 2001; Hoffman et al., 2017). Sedimentary metallogenesis, especially the precipitation of iron (Fe) and manganese (Mn, this study), were largely governed by these factors (Roy, 2006; Bekker et al., 2010; Maynard, 2010).

The formation of Mn deposits was initiated from the Mesoarchean, and these were abundant during the Paleoproterozoic, and were subsequently revived in the late Neoproterozoic (Roy, 2006; Maynard, 2010; Yu et al., 2016; Xiao et al., 2017; De Putter et al., 2018; Smith and

* Corresponding author.
E-mail address: nnzhongxp@cup.edu.cn (N. Zhong).

https://doi.org/10.1016/j.precamres.2023.107091
Received 24 November 2022; Received in revised form 29 March 2023; Accepted 12 May 2023
Available online 28 May 2023

Beukes, 2023; Smith et al., 2023). Sedimentary Mn deposits are sometimes huge (hundreds of million tons), such as the ~2.4 Ga banded iron formation-hosted Kalahari Manganese Field in South Africa, which holds ~4,200 Mt of Mn metal (mainly as Braunite-Kutnahorite phases) and represents over 70 % of the world's known land-based Mn resources (Beukes et al., 2016; Gumsley et al., 2017). Some of the sedimentary Mn deposit hosted in the organic-rich sediments were developed on the margins of euxinic basins as oxide–carbonate phases under a greenhouse–icehouse climate (Calvert and Pedersen, 1996; Roy, 2006; Maynard, 2010; Cabral et al., 2011; Yu et al., 2019). During the Cryogenian period (ca. 720–635 Ma) there were multiple ice ages, of which the Sturtian (ca. 720–660 Ma) and the Marinoan (ca. 650–635 Ma) deposited glaciogenic sediments to low-latitude areas (Hoffman et al., 1998; Hoffman and Schrag, 2002). Most of the Neoproterozoic Mn deposits were formed in a stratified ocean that developed during the interglacial stages. The interglacial times are generally characterized by episodes of marine transgression–regression and elevated atmospheric oxygen levels due to increased burial of organic matter (Fan et al., 1992; Klein and Ladeira, 2004; Yu et al., 2016). The advent of free O_2 in the Earth surface system allowed more efficient geobiological cycling of metals regardless of whether the reactions were favoured by microbial activity or not (Planavsky et al., 2014; Havig et al., 2015; Gumsley et al., 2017).

Tectonic rifting during the breakup of supercontinents may have led to the introduction of hydrothermal Mn and Fe to marine basins (Barley and Groves, 1992; Roy, 2006). Unlike modern Mn nodules that primarily contain Mn(IV) oxides, the ancient Mn deposits were generally dominated by the Mn(II) mineral phases, particularly as rhodochrosite ($MnCO_3$), kutnohorite ($(Ca,Mn)(CO_3)_2$), and Mn-calcite (Mn-$CaCO_3$). Examples include the Neoproterozoic Mn-carbonate ores hosted in the Datangpo Formation black shales (South China) and in Urucum (Brazil), the Carboniferous Mn-carbonate ores in the Masi Formation (South China), and the Jurassic Mn-carbonate ores in the Úrkút Formation (Hungary) (Polgári et al., 2012a; Yu et al., 2019; Biondi et al., 2020; Yu et al., 2021). Rarely, Neoproterozoic Mn deposits in Namibia and Brazil consist of Mn oxides with interstratified banded iron formations (Klein and Ladeira, 2004; Cabral et al., 2011).

It has been widely suggested that microorganisms may play a vital role in metal ore formation, including Mn, Fe and U (Konhauser et al., 2002; Sánchez-Román et al., 2014; Zhao et al., 2018; Polgári et al., 2019; Yu et al., 2019; Biondi et al., 2020). Most Mn-carbonate ores in the sedimentary rock record are assumed to have formed by diagenetic reduction of precursor Mn oxides in anoxic sediments underlying permanently or transiently oxygenated basins (Calvert and Pedersen, 1996; Huckriede and Meischner, 1996; Yu et al., 2019; Polgári and Gyollai, 2021). A dual role of microorganisms in Mn-carbonate ore formation has been suggested: (1) microbial oxidation of Mn(II) and reduction of Mn(IV) oxides; (2) as nucleation site for Mn minerals (Polgári and Gyollai, 2021; Huang et al., 2022). Recent studies have proposed an alternative genesis model for Mn-carbonate ores, suggesting that aqueous Mn(II) may bind with CO_3^{2-}(aq) that is derived from dissolved carbonate originating from surface waters to develop primary Mn carbonate phases (Herndon et al., 2018; Wittkop et al., 2020).

Despite decades of research interest, Mn carbonates with micrometre-scale ooid-like structures have rarely been reported. Huang et al. (2022) observed Mn carbonates with spheroidal-shaped morphology (5–10 μm) and core–shell structures in the giant Malkansu Mn metallogenic belt at West Kunlun (Northwest China), and demonstrated the direct role of microbes in Mn carbonate formation. Zhang et al. (2021) reported the microbial metallogenesis of spherical and ellipsoidal rhodochrosite (about 50–400 μm) cemented by kutnohorite in the Doushantuo Formation (South China) that was deposited after the Marinoan glaciation. However, the formation mechanism of the Mn deposits in the lower member of the Datangpo Formation (DTP-1) (ca. 660 Ma) in South China, which formed between the Sturtian and Marinoan Snowball Earth events, still remains a matter of debate (Fan et al., 1992; Zhou et al., 2013; Yu et al., 2016; Xiao et al., 2017; Yu et al., 2019). The Mn deposits that occur in the DTP-1 were originally proposed to be formed through solely redox-controlled processes in possibly transiently oxidised seawater during the interglacial period (Zhang et al., 2015a; Wu et al., 2016; Xiao et al., 2017). Yu et al. (2019) provided new evidence for microbially-mediated processes that controlled the DTP-1 Mn carbonates. However, the micro-scale (i.e., several μm) ooidal texture of the DTP-1 Mn carbonates has seldom been reported, and its nuanced formation pathway is poorly constrained (Fan et al., 1999). In this study, detailed petrography and geochemical analyses were carried out to reassess biogeochemical pathways in regulating the formation of black shale-hosted micro-ooidal Mn-carbonate deposits in South China, which may shed light on the global Neoproterozoic post-glacial carbon cycle under specific atmospheric-oceanic conditions.

2. Geological settings and samples

The Late Neoproterozoic Nanhua Basin in South China was developed as a rift basin along the southern margin of the Yangtze Platform (Fig. 1a) during the breakup of the Rodinia Supercontinent at about 820 Ma (Li et al., 1999; Wang and Li, 2003). In chronological order, the Cryogenian successions in South China are the Qianzimen/Tiesi'ao/Fulu formations (Sturtian-age tillites), the Datangpo Formation, and the Nantuo Formation (Marinoan-age tillites) (Fig. 1b). The geological age of the Datangpo Formation is constrained between 663 ± 4 Ma and 654.5 ± 3.8 Ma by a pair of zircon U–Pb dates that were derived from interbedded tuff layers in the bottom and top parts of the Datangpo Formation (Zhang et al., 2008).

The Datangpo Formation thus represents a post-Sturtian interglacial interval, and can be divided into two members. The lower member (the DTP-1) is composed of carbonaceous black shales and interbedded massive or laminated Mn carbonates near the base (Fig. 1c) (Wang and Li, 2003; Zhang et al., 2008). The upper member of the Datangpo Formation (DTP-2) is composed of several hundred meters of siltstone (Fig. 1c). Fresh drill core of the Datangpo Formation was sampled from the ZK0408 borehole in the Xiushan district, ESE of Chongqing, South China (Fig. 1a), including Mn-rich samples and adjacent black shales (Fig. 1c). In addition, five other Mn-rich samples were collected from a manganese mining block, on which the ZK0408 borehole was located (Fig. 1c). The ZK0408 borehole was drilled to confirm the resource reserve of the Mn ore, so therefore both the Mn-rich samples from ZK0408 and the five Mn-rich mining block samples were from the same ore body. The paleogeographic settings of the Nanhua Basin during deposition of the Datangpo Formation have been reconstructed by estimating the relative water depths that were reflected by the spatial distribution of the overlying Nantuo Formation tillite (Wang and Li, 2003) (Fig. 1a). It has been suggested that the wide range of water depths was determined by a series of horsts and grabens formed by axis-parallel faults that prevailed along the general present-day northwest-to-southeast axis of the Nanhua Basin (Wang and Li, 2003; Yu et al., 2017). The studied section was likely deposited in a structural graben developed along the mid-slope of the Nanhua Basin (Jiang et al., 2006; Yu et al., 2017), where the thickness of the DTP-1 is ~21 m, with a ~3 m thick manganese-rich layer.

3. Methods

3.1. Time-of-flight secondary ion mass spectrometry

Time-of-flight secondary ion mass spectrometry (ToF-SIMS) scans a surface with a high energy ion beam (Vickerman and Briggs, 2013). In addition to mass spectra, ion images are also obtained. The chemical data in these ion images can be matched with morphological structures in optical and electron micrographs. The samples for ToF-SIMS analyses were prepared as slabs cut with a combusted and solvent-cleaned saw blade. During the cutting process, the saw blade was cooled and lubricated by Milli-Q water, which was gravity fed to the saw blade and

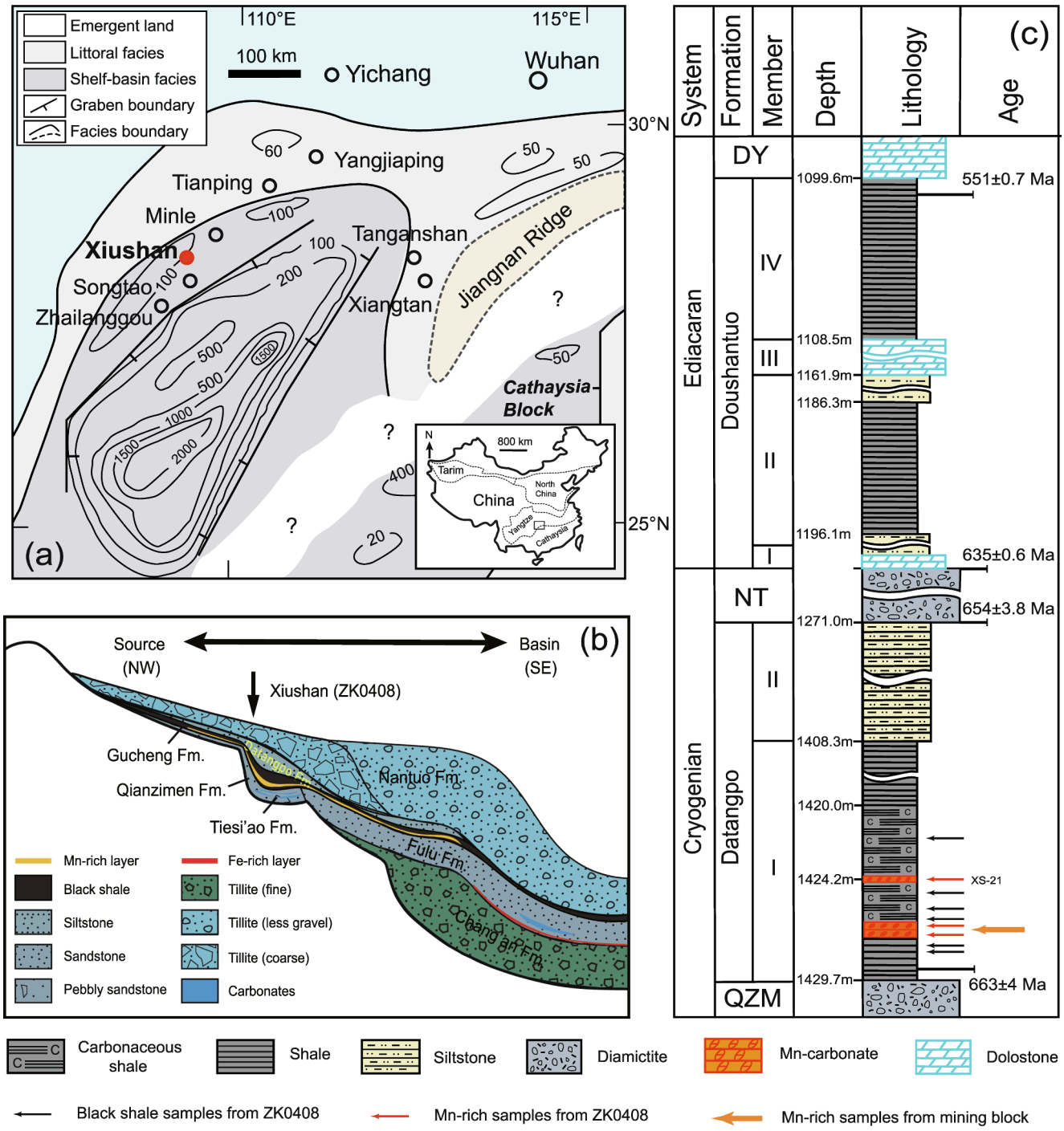

Fig. 1. Geological setting of the Late Neoproterozoic Nanhua Basin in South China. (a) Sedimentary lithofacies, paleogeographic and paleobathymetric map of the Nanhua Basin during glacial deposition of the Nantuo Formation, modified after Li et al. (2012). (b) Neoproterozoic stratigraphic sequence and sedimentary section of the Nanhua Basin, modified after Wang (2022). Sturtian-age tillites are the Qianzimen, Tiesi'ao, Gucheng, and Fulu formations. (c) Stratigraphic column of the ZK0408 borehole from the Xiushan district. The radioactive ages of 551.1 ± 0.7 Ma, 635.2 ± 0.6 Ma, 654.5 ± 3.8 Ma and 663 ± 4 Ma are from Condon et al. (2005), Zhang et al. (2005), Zhang et al. (2008) and Zhou et al. (2004), respectively. QZM = Qianzimen Formation, NT = Nantuo Formation, DY = Dengying Formation, Fm. = formation.

subsequently disposed of after single use to minimise anthropogenic contamination.

Analyses were performed on a ToF-SIMS IV instrument (ION-TOF GmbH, Germany) located at the RISE Research Institute of Sweden in Borås, Sweden. Samples were analysed by rastering a 25 keV Bi_3^+ beam over a 60 × 60 to 500 × 500 μm^2 area for 250–700 s. The analyses were performed in both positive and negative mode at high mass resolution (bunched mode: m/Δm ≥ 5000 at *m/z* 30, Δl ~5 μm) with a pulsed current of 0.1 pA. In addition, spectra were collected at high spatial resolution (burst alignment mode: m/Δm ~100–300, Δl < 1 μm) with a pulsed current of ~0.045 pA. As the samples were insulating, the sample surface was flooded with electrons for charge compensation.

3.2. Carbon isotope measurements

The samples were sawn to remove exterior surfaces, prior to being

ground into rock powders using a micro ball mill (Grinder GT200) and agate grinding jars, which were cleaned with baked sand, Milli-Q water (3 times) and methanol (3 times) between samples. The interior core samples were powdered and then reacted with phosphoric acid at 75 °C for 72 h for Mn carbonate enriched samples or at 25 °C overnight for normal black shales to produce CO_2, which was cryogenically distilled from the reaction vessel and introduced to a stable isotope ratio mass spectrometer to analyse inorganic carbon isotope ($\delta^{13}C_{carb}$) and oxygen isotope ($\delta^{18}O$) ratios. The national standards GBW04405 and GBW04406 were applied to correct the $\delta^{13}C_{carb}$ and $\delta^{18}O$ ratios, and yielded analytical precisions of $<\pm0.2$ ‰ and $<\pm0.3$ ‰, respectively. The $\delta^{13}C_{carb}$ and $\delta^{18}O$ measurements were conducted on a MAT253 mass spectrometer at the State Key Laboratory of Petroleum Resources and Prospecting at China University of Petroleum-Beijing. Kerogen isolation and analysis for its carbon isotopes ($\delta^{13}C_{org}$) were performed using an Isotope Ratio Mass Spectrometer (Thermo Scientific 253 Plus) at the Research Institute of Petroleum Exploration and Development (Langfang Branch).

3.3. Scanning electron microscopy and energy-dispersive spectroscopy

Scanning electron microscopy and energy-dispersive spectroscopy (SEM-EDS) was performed using a FEI Helios NanoLab™ 650 Dual-Beam™ focused ion beam scanning electron microscope in secondary electron and backscattered electron modes. Images were acquired from argon ion polished specimens using an accelerating voltage of ~15 kV and working distances of ~10 mm for best spatial resolution and ~9 mm for elemental analysis. Element mapping was performed using a Bruker XFlash 6130 energy-dispersive spectroscopy system.

Additional SEM images were obtained at the RISE Research Institute of Sweden, using a Supra 40 VP FEG SEM (Zeiss, Germany) at high vacuum (7×10^{-7} mbar) operating at 1 keV in secondary electron mode.

3.4. Organic petrography and cathodoluminescence petrography

The organic petrography was carried out on polished surfaces of epoxy embedded rock sections using a Leica microscope equipped with a CRAIC microscope photometer with reflected light (546 nm wavelength) under a 50 × oil-immersion objective. Cathodoluminescence microscopy was performed on a cold cathode instrument (BII CLF-2, Canada) with an acceleration voltage of 13–14 kV, and a beam current of 250–300 μA.

3.5. Trace and major elemental analyses

Powdered bulk rock samples (<200 mesh) were measured for both major and trace elemental concentrations at the State Key Laboratory of Ore Deposit Geochemistry, Institute of Geochemistry, Chinese Academy of Sciences, Guiyang. Major element oxides were determined using the Thermo Fisher ARL Perform'X 4200 X-ray fluorescence spectrometry (XRF). About 800 mg of dried (105 °C, 2 h) powdered samples were mixed with flux (Li_3BO_3:$LiBO_2$ = 66:34) at a 1:10 wt ratio and fused at 1050 °C. The analytical precision of the XRF was better than 5 %.

The concentrations of trace elements (including rare earth elements) were determined using inductively coupled plasma mass spectrometry (Plasma Quant MS Elite ICP-MS, Jena, Germany). About 100 mg powdered sample was weighed into a polytetrafluoroethylene bomb and digested in a reagent mixture of 1 mL of HF (38 % v/v) and 0.5 mL of HNO_3 (68 % v/v). The sealed bombs were placed in an oven and heated at 200 °C for 12 h. After cooling, 1 mL of a 1 μg/mL Rh solution was added into the cooled solution as an internal standard to correct for matrix effects and instrument drift. The opened bombs were then heated on a hot plate at 150 °C to be evaporated to dryness. This was followed by twice adding aliquots of 1 mL HNO_3 (68 % v/v) and evaporating to dryness, in order to remove most of the silica. The residue was re-digested by adding 6 mL of HNO_3 (40 % v/v) and heated in an oven at 140 °C for 3 h before being transferred to a 100 mL volumetric flask for testing. The detection limit for trace elements ranged from 0.001 μg/L to 0.2 μg/L. Single-element stock solutions (1000 mg/L) were prepared using pure metals or pure metal oxides. Three multi-element stock solutions containing 10 mg/L of each analyte were prepared: (1) Li, Be, V, Cr, Co, Ni, Cu, Zn, Ga, Rb, Sr, Cs, Ba, Pb, Th, U; (2) Sc, Y and fourteen REEs; and (3) W, Mo, Nb, Ta, Zr, Hf. The stock standard solutions (1) and (2) were prepared in 3 % v/v HNO_3, and the stock standard solution (3) was prepared in 2 % v/v HNO_3 and 0.2 % v/v HF. The multi-element working standards made from the three stock solutions were prepared with concentrations spanning 10–100 μg/L, at which level all the trace elements could be mixed together. The trace element measurements yielded an analytical precision of <5 %.

4. Results

4.1. Petrographic characteristics

The Datangpo Formation Mn-carbonate ores mainly display rhythmic laminae texture or massive texture in hand specimen (Fig. 2a and 2b). The Mn-carbonate ores with rhythmic laminae occur predominantly in the lower part of the DTP-1 Mn layer. These laminae have alternations of organic-rich and Mn-rich composition. Calcium sulfate ($CaSO_4$) crystals, which have radial, fibrous flower-like structures with diameters of 50–100 μm, were mainly observed in the Mn-rich lamina of these Mn-carbonate ores (Fig. 2c). These might be authigenic gypsum formed from pore water. The Mn in these enriched black shales in the DTP-1 occurs dominantly as rhodochrosite and Ca-rhodochrosite (Ca < 10 wt%). The Mn-carbonate crystals have different morphological characteristics in the laminated- and massive Mn-carbonate ores. SEM investigation of etched laminated Mn-carbonate ore samples revealed that they are mainly characterised by micro-spherical Mn carbonate grains with diameters of 3–5 μm (referred to as Type I, Fig. 2d and Fig. 3a-b). In contrast, the Type II Mn-carbonate grains in the massive Mn-carbonate ores display short rod-like shape (or axiolitic shape) with relatively small diameters of <2 μm (Fig. 2e, 2f and Fig. 4a). In addition, at high magnification the Type II Mn-carbonate grains have a rhombus-shaped scaly texture (Fig. 2f).

Under back-scattered electron mode, the spheroidal Type I Mn-carbonate has microspherolitic microstructures with radial-concentric microfabrics, and rings of organic matter associated with specific laminae (Fig. 3b and 3c). There are signs of growth banding in the Type I Mn-carbonates, in the form of alternating light and dark laminae, which mainly express variations in Ca and Mn concentrations (Fig. 3d and 3e). The cores of individual ooidal-shape microspheres are more enriched in Ca relative to other layers. The Ca-rich cores are coated with a kerogen ring, and some cell-like structures are preserved as micro-cavities in the microspherolitic structures (Fig. 3b and 3c). A Mn-rich layer (rhodochrosite) coats the kerogen-cavity ring, and in turn is coated by an outer layer of Ca-rhodochrosite (Fig. 3b and 3e). The Mn microspheres generally cluster together to form amalgamations with diameters of 20–50 μm. The Mn microspheres are predominantly surrounded and/or cemented by an organic matrix (i.e., carbonaceous matter). The organic matter can be distinguished by greyish yellow colour under reflected light using an oil-immersion objective (Fig. 3a), and by dark spots under SEM (Fig. 3b and 3c). Selective elemental mapping (Fig. 3f), and coupled distribution of C—N—H elements revealed by ToF-SIMS (Fig. 5) helps demonstrate the occurrence of organic matter within or around the Type I Mn microspheres as an organic matrix.

In contrast, the short rod-shaped Mn carbonate grains are mainly embedded in a calcite matrix (Fig. 4a), or occasionally in silica (Fig. 4c, 4i). The Type II Mn-carbonate grains generally have a core–shell structure, instead of the multiple cycles of growth banding observed in the Type I Mn-carbonate (Fig. 4c). The calcite (or Mn-calcite) cores are surrounded by (Ca-)rhodochrosite concentric shells. The organic matter in the Type II Mn-carbonate ore fills in the intergranular pores of the

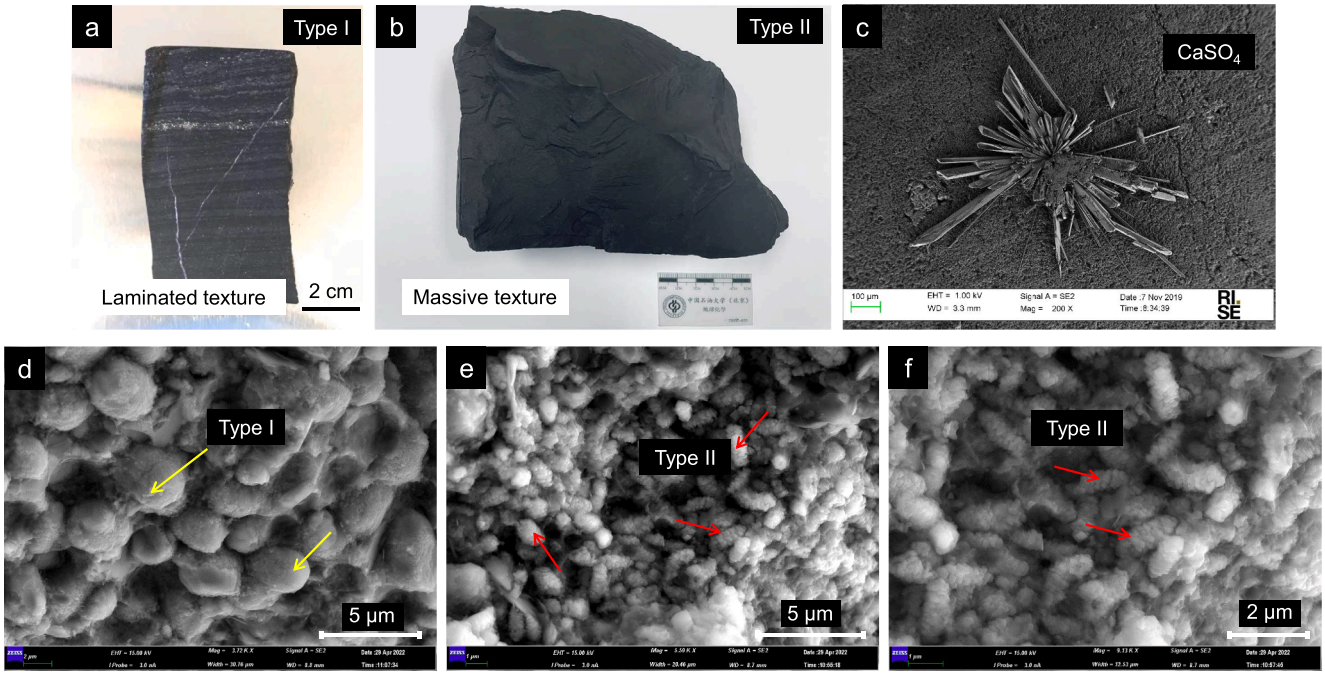

Fig. 2. (a) and (b) Photographs of representative samples from the Cryogenian interglacial DTP-1 Mn carbonate ore layer in South China, showing a laminated texture (XS-15, 1426.75 m) and a massive texture (MK-3 from the mining block). (c) Representative scanning electron microscope photomicrograph of gypsum ($CaSO_4$) with radial, fibrous flower-like structures, observed predominately in the Mn-rich samples with laminated structure (sample XS-15). (d–f) Scanning electron microscope images of DTP-1 Mn-ore samples as etched slabs; (d) sample MK-2, (e and f) sample XS-21. Mn-carbonate crystals with spheroidal shape (see d, referred to as Type I) are present in the laminated samples, and Mn-carbonate crystals with short-rod shape (or axiolitic shape) (see e, referred to as Type II) are present in the massive samples. (f) Enlarged image of (d), showing the rhombus-shaped scaly texture of the Type II Mn-carbonate crystals.

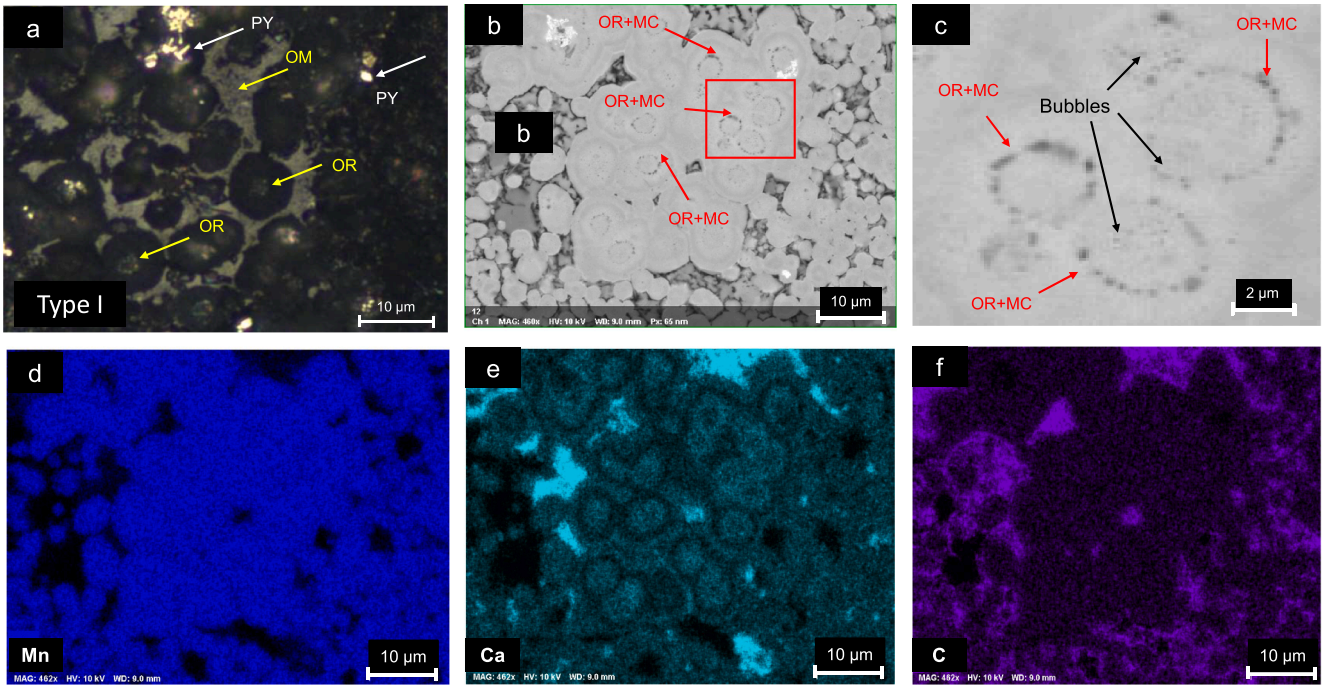

Fig. 3. (a) Organic petrography photomicrograph of a polished block of the Mn-rich sample MK-2 under a 50 × oil immersion objective. Organic matter has a greyish-yellow colour (i.e., yellow arrows; OR = organic ring, OM = organic matter preserved in intergranular pores as organic matrices), and can be observed as an organic-rich ring in each Mn carbonate grain. PY = pyrite. (b) and (c) Scanning electron micrographs of a Mn carbonate cluster in the MK-2 sample, showing their micro-ooidal texture. Black organic-rich rings, cell-like cavities (i.e., red arrows; MC = micro-cavity), and gas bubbles can be observed within the middle of the Mn-carbonate grains. (d–f) Selective element maps of the same field of view of the MK-2 sample as in (b), showing Mn, Ca and C, respectively. Due to the relatively low resolution, the organic-rich rings in the Mn-carbonate grain (b) are not able to be distinguished by element mapping in (f). Most of the organic matter in (f) is likely to be an organic residue after oil cracking. (For interpretation of the references to colour in this figure legend, the reader is referred to the web version of this article.)

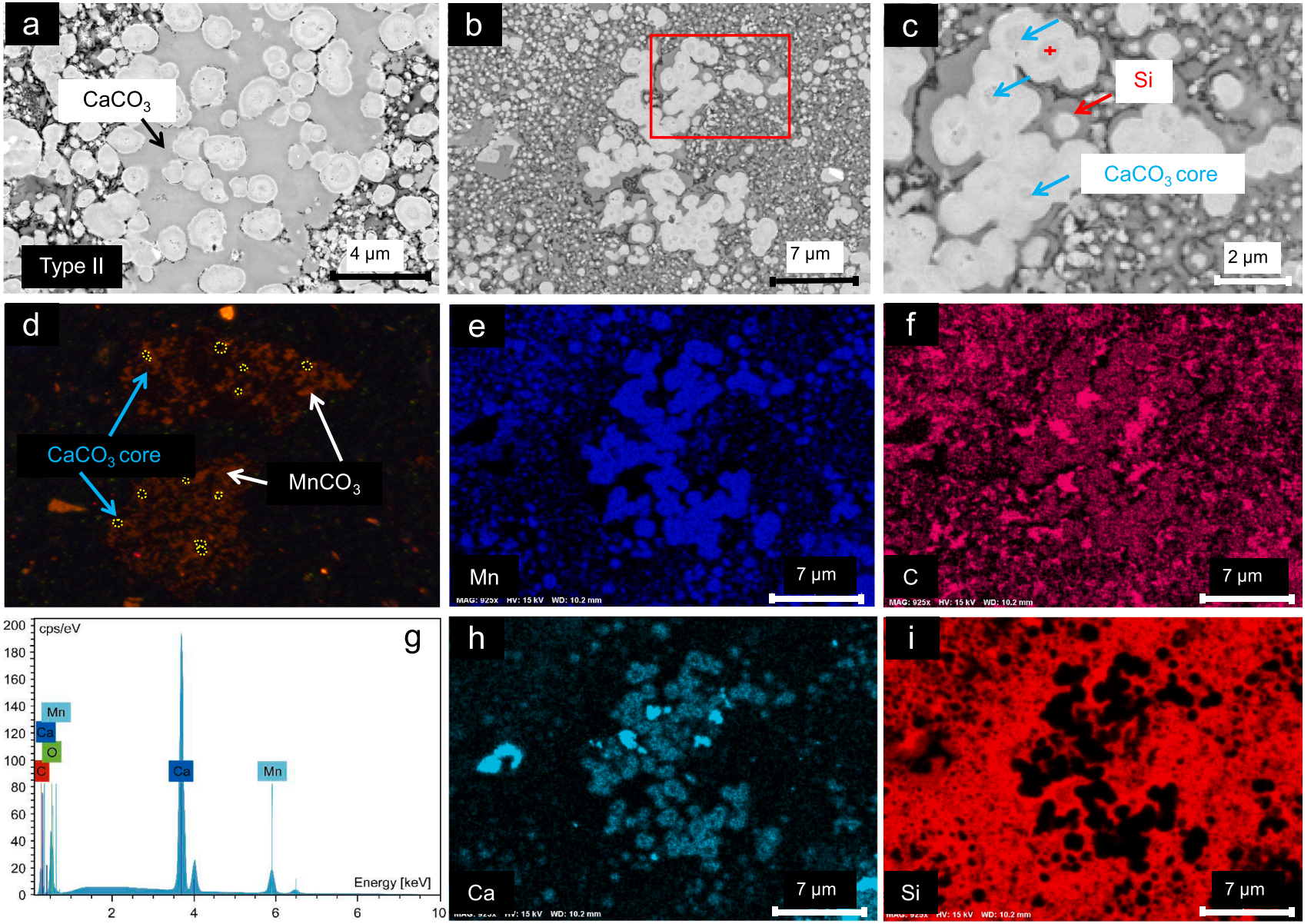

Fig. 4. Micro-textural features of the Type II Mn carbonate (sample XS-21). (a) and (b) Scanning electron micrographs of the Type II Mn carbonate grains embedded in calcite and silicon, respectively. The grain size is relatively small, <2 μm. (c) Enlarged area on (b) (the red rectangle); (d) Typical cathodoluminescence image of Type II Mn carbonate. The fine-grained rhodochrosite has a reddish-orange luminescence colour. The $CaCO_3$ cores do not display a bright luminescence colour, and are highlighted by yellow-dashed circles. (e, f, h, i) Element maps of the same field of view of the XS-21 sample as in (b), showing Mn, C, Ca, and Si, respectively. (g) EDS spectra with identifications to confirm the mineralogy as Ca-carbonate, taken on the target point (red cross) in (c). (For interpretation of the references to colour in this figure legend, the reader is referred to the web version of this article.)

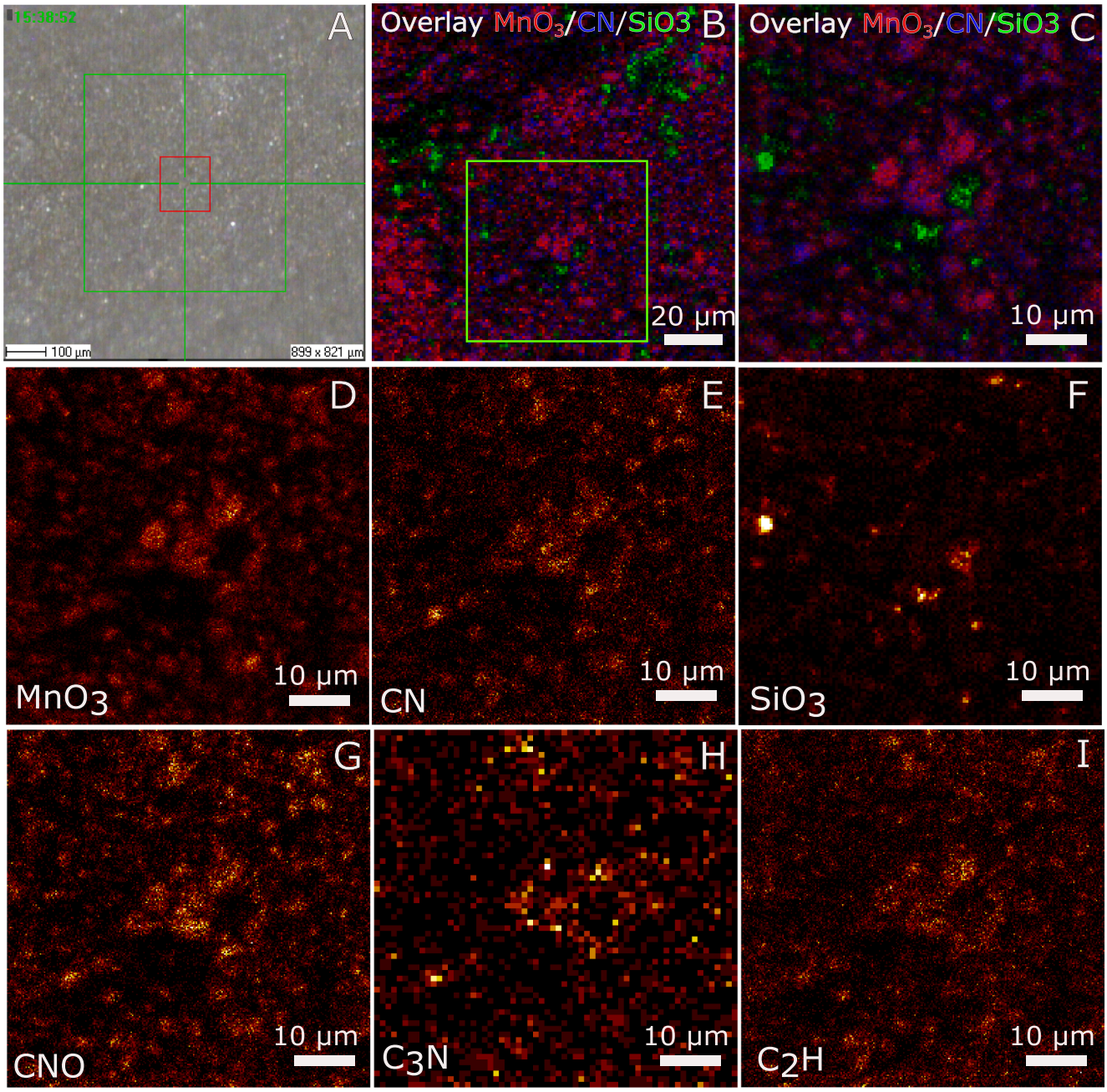

Fig. 5. Time-of-flight secondary ion mass spectrometry (ToF-SIMS) data of a Mn-rich sample (MK-2) from the Datangpo Formation. A) ToF-SIMS video image. The red square indicates the area of analysis for the ion image in B). B–C) Overlays of the negative high spatial resolution ion images of MnO_3^- (red), CN^- (blue) and SiO_3^-. The green square in B indicates the zoomed-in area shown in C. D–I) Negative high spatial resolution ion images of MnO_3^-, CN^-, SiO_3^-, CNO^-, C_3N^- and C_2H^-, respectively. (For interpretation of the references to colour in this figure legend, the reader is referred to the web version of this article.)

grains, or around the aggregates (Fig. 4a, 4b, 4c and 4f). Bubble-like structures can be observed in both the Type I and Type II Mn-carbonate, predominately distributed in the cores and in the organic ring laminae of the Type I Mn-carbonate grains.

4.2. ToF-SIMS

ToF-SIMS ion images show co-localisation of the signals of organic matter (here represented by CN^-, CNO^-, C_3N^- and C_2H^-) with the signals from the manganese carbonates (MnO_3^-), but not with the signals of the silicates (SiO_3^-) (Fig. 5). When zooming in on specific areas it can be observed that the organic signals appear quite patchy within the Mn-carbonates.

4.3. Elemental compositions

Major element compositions of the samples are shown in Table 1. The Mn content of the DTP-1 Mn-carbonate ores varies from 12 to 27 wt %. The Mn-rich black shales are enriched in Ca and Mg and depleted in Si, Al, K and Ti compared with the adjacent normal black shales. The composition and PAAS-normalised distribution of selected trace elements in the samples are shown in Table S1 and Fig. S1. The Mn-rich black shales are enriched in Co, Mo and Sr, and depleted in V, Cr, Cu, Rb, Zr, Ba and Th. The adjacent black shales are selectively more enriched in Mo, U and V compared with the Mn ores. The black shales are relatively enriched in total REE (148–659 ppm, average = 293 ppm) compared with the Mn-rich samples (106–246 ppm, average = 172

Table 1
Major element and inorganic carbon isotopic compositions of the Mn-rich samples (Mn-BS) and the associated black shales (BS) from the lower member of the Datangpo Formation in South China.

Samples	Lithology	Depth (m)	TOC (wt. %)	$\delta^{13}C_{carb}$ (‰)	SiO_2 (wt. %)	Al_2O_3 (wt. %)	MgO (wt. %)	CaO (wt. %)	Na_2O (wt. %)	K_2O (wt. %)	TiO_2 (wt. %)	P_2O_5 (wt. %)	Fe (wt. %)	Mn (wt. %)	LOI (wt. %)	Mn/Fe (mol/mol)
MK-1	Mn-BS	n.d.	1.78	−8.9	21.0	4.3	3.2	7.2	1.43	1.00	0.37	0.23	2.2	22.6	29.2	10.4
MK-2	Mn-BS	n.d.	5.7	−9.5	8.2	1.43	4.4	9.2	1.04	0.37	0.20	0.18	1.45	26.9	38.2	18.9
MK-3	Mn-BS	n.d.	1.6	−6.6	8.8	1.54	2.8	15.0	1.08	0.42	0.16	1.17	2.2	24.9	32.7	11.8
MK-4	Mn-BS	n.d.	1.00	−9.1	34.5	7.4	2.1	4.7	1.15	1.92	0.48	0.31	8.0	12.2	21.7	1.56
MK-5	Mn-BS	n.d.	3.2	−9.6	21.8	3.2	3.6	6.9	1.21	0.84	0.28	0.27	1.79	24.3	29.3	13.8
XS-27	BS	1421.83	3.9	−5.6	58.4	15.9	1.11	0.66	1.55	3.8	0.69	0.16	4.3	0.75	7.7	0.18
XS-21	Mn-BS	1424.23	1.49	−6.5	22.6	5.0	3.0	11.1	1.04	1.55	0.15	0.19	5.6	16.5	28.3	3.0
XS-19	BS	1424.83	4.0	n.d.	70.8	10.8	0.69	1.57	1.54	2.35	0.32	0.89	2.3	0.41	7.9	0.19
XS-17	BS	1425.95	1.57	−6.2	52.2	22.3	1.13	1.28	0.59	6.3	0.36	0.67	3.0	0.96	8.2	0.33
XS-16	BS	1426.45	1.37	−6.9	60.8	16.8	0.91	0.54	1.69	3.9	0.66	0.22	3.1	0.16	7.8	0.05
XS-15	Mn-BS	1426.75	1.37	−7.2	18.9	3.4	3.5	12.8	1.04	0.90	0.21	0.61	2.5	19.8	30.4	8.1
XS-14	Mn-BS	1427.20	0.55	−8.0	7.78	1.15	8.3	19.9	0.86	0.28	0.10	0.30	1.31	18.1	34.2	14.1
XS-11	BS	1427.70	0.83	−6.1	61.0	13.0	1.11	4.7	1.11	3.2	0.58	1.27	2.2	1.78	7.5	0.81
XS-10	BS	1428.00	0.27	−6.8	60.2	14.5	0.99	3.5	1.48	3.4	0.71	0.15	3.0	1.46	9.7	0.49

TOC = total organic carbon; LOI = loss-on-ignition; n.d. = not determined.

ppm) (Table S1). PAAS-normalised REE of most of the Mn-rich shales are characterised by unusual positive Ce anomalies (Ce/Ce* = 1.08–1.34, average = 1.24), which are absent from the adjacent black shales (0.92–0.94, average = 0.93) (Fig. 6a, 6c and 6d; Table S1). In addition, the positive Ce anomalies in the Mn-rich shales have a positive correlation with Mn content (Fig. 6b). However, one Mn-rich sample (XS-21, with a Mn content of 16.5 wt%) does not have a positive Ce anomaly (Ce/Ce* = 0.98) (Fig. 6a, 6b and 6d; Table S1). The Mn-rich black shales are relatively enriched in medium-REEs and heavy-REEs from Gd to Lu. Slightly positive Eu anomalies (average = 1.33) (Table S1) and a positive correlation of Mn with Eu/Eu* (Fig. S2) were observed in most of the Mn-rich samples in the DTP-1. Here Ce/Ce*, Eu/Eu* and Pr/Pr* are defined as $2Ce_{SN}/(La_{SN} + Pr_{SN})$, $2Eu_{SN}/(Sm_{SN} + Gd_{SN})$ and $2Pr_{SN}/(Ce_{SN} + Nd_{SN})$ respectively, as proposed by Bau and Dulski (1996), where *SN* represents normalization to the Post Archean Australian Shale (PAAS) (Taylor and McLennan, 1985).

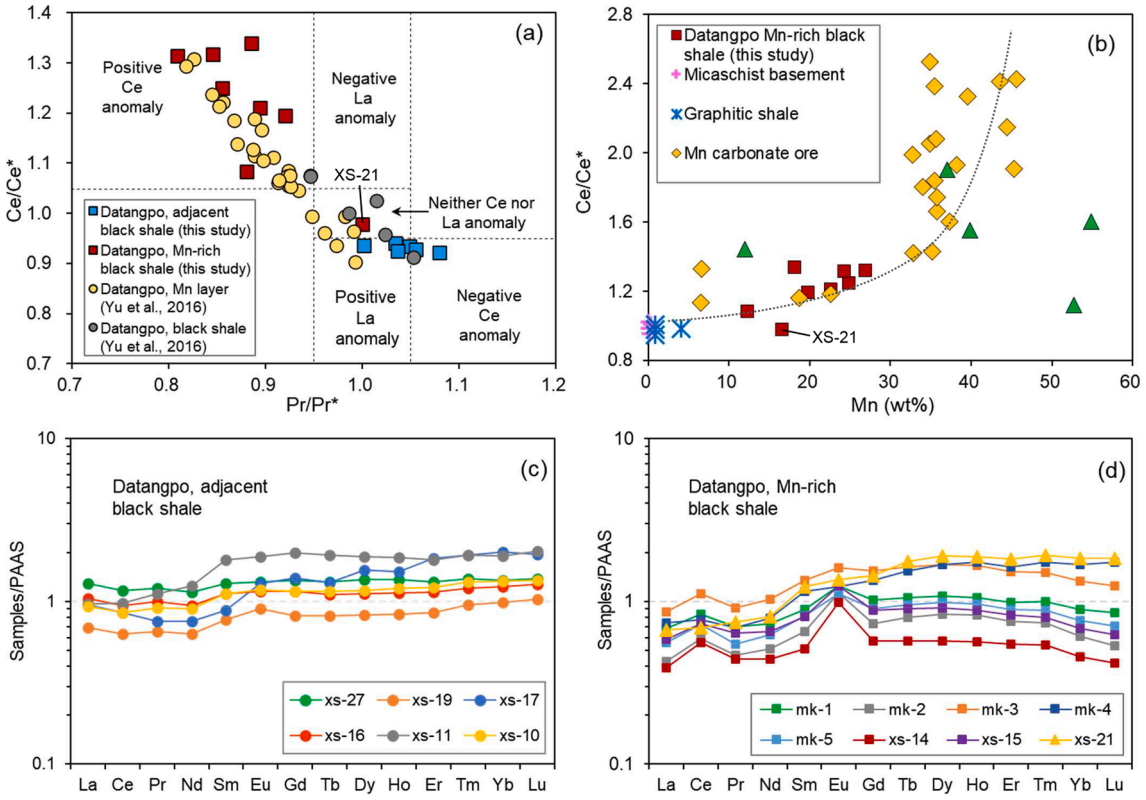

Fig. 6. (a) Cross plot of Pr/Pr* versus Ce/Ce*. A positive Ce anomaly is clear for the Mn-rich samples, and is absent for the adjacent black shales. $Pr/Pr^* = 2Pr_{SN}/(Ce_{SN} + Nd_{SN})$, $Ce/Ce^* = (2Ce_{SN}/(La_{SN} + Pr_{SN})$. SN represents normalization to the Post Archean Australian Shale (PAAS) (Taylor and McLennan, 1985). The different anomaly fields are after Bau and Dulski (1996). (b) Cross plot of Mn (wt%) versus Ce/Ce*, showing a positive correlation that is interpreted to have resulted from the oxidation of Ce by Mn oxide/hydroxide, and/or adsorption of Ce(IV) on the surfaces of Mn oxide/hydroxide. Literature data are from De Putter et al. (2018). (c) and (d) The PAAS-normalized REE distribution for adjacent black shales and Mn-rich shale samples from the Cryogenian Datangpo Formation in South China, respectively.

4.4. Carbon isotope ($\delta^{13}C_{carb}$ and $\delta^{13}C_{org}$) data, and comparison to literature values

Bulk $\delta^{13}C_{carb}$ values of the Datangpo Formation Mn-rich black shales are relatively depleted in ^{13}C, ranging from −6.5 to −9.6 ‰ with an average of −8.2 ‰ (Table 1). Such a negative $\delta^{13}C_{carb}$ composition is comparable with Ca-rhodochrosite preserved in the Lower Carboniferous Rheno-Hercynian zone ($\delta^{13}C_{carb}$ = −6 to −10.5 ‰) and the Holocene Baltic Sea ($\delta^{13}C_{carb}$ = −6 to −12.6 ‰) (Huckriede and Meischner, 1996), and with previously published $\delta^{13}C_{carb}$ data for Mn-carbonates in the Xiushan section, South China (Wu et al., 2016) (Fig. 7). The $\delta^{18}O_{carb}$ values of the studied Mn-rich black shales are intermediate between the Ca-rhodochrosite from the Lower Carboniferous Rheno-Hercynian zone and the Holocene Baltic Sea (Huckriede and Meischner, 1996) (Fig. 7). In contrast, the adjacent black shale samples are relatively more depleted in ^{18}O and enriched in ^{13}C compared with the studied Mn-rich samples and those from the younger settings (Fig. 7).

5. Discussion

5.1. Initial precipitation phase of Mn

The paleogeographic context in response to supercontinent evolution and geochemical characteristics have previously demonstrated the predominant hydrothermal origin of Mn^{2+} in the Cryogenian interglacial Nanhua Basin (Wu et al., 2016; Yu et al., 2016; Zhou et al., 2016; Xiao et al., 2017). This is supported by data from this study, including significantly high Mn/Fe ratios (3–18.6; average = 10.1) (Table 1), positive Eu anomalies (average = 1.33) (Fig. 6d; Table S1), and high Fe/Ti ratios coupled with low Al/(Al + Fe + Mn) ratios (Fig. S2) (see more details in supplementary information).

Most ancient Mn deposits have undergone varying degrees of diagenesis and metamorphism after burial (Maynard, 2010). Therefore, identifying the original precipitated phase of Mn deposits is critical for understanding the formation mechanism of the Mn carbonate, the biogeochemical cycling of Mn and C, and how they reflect the chemical state of ancient seawater. Herndon et al. (2018) advanced a hypothesis that Mn carbonates may nucleate in redox stratified water columns, linked to Ca-carbonate dissolution. This mechanism has received increased attention in latest studies (Wittkop et al., 2020; Chen et al., 2022; Gao et al., 2021). Alternatively, Mn can initially be oxidised to Mn oxide/hydroxide, which may subsequently be converted into Mn carbonates by diagenesis after burial in organic-rich sediments, during which process microbes may play an important role in regulating the redox cycling of the Mn (Tebo et al., 2004; Learman et al., 2011; Polgári et al., 2012a; Polgári et al., 2012b; Yu et al., 2019; Smith et al., 2023).

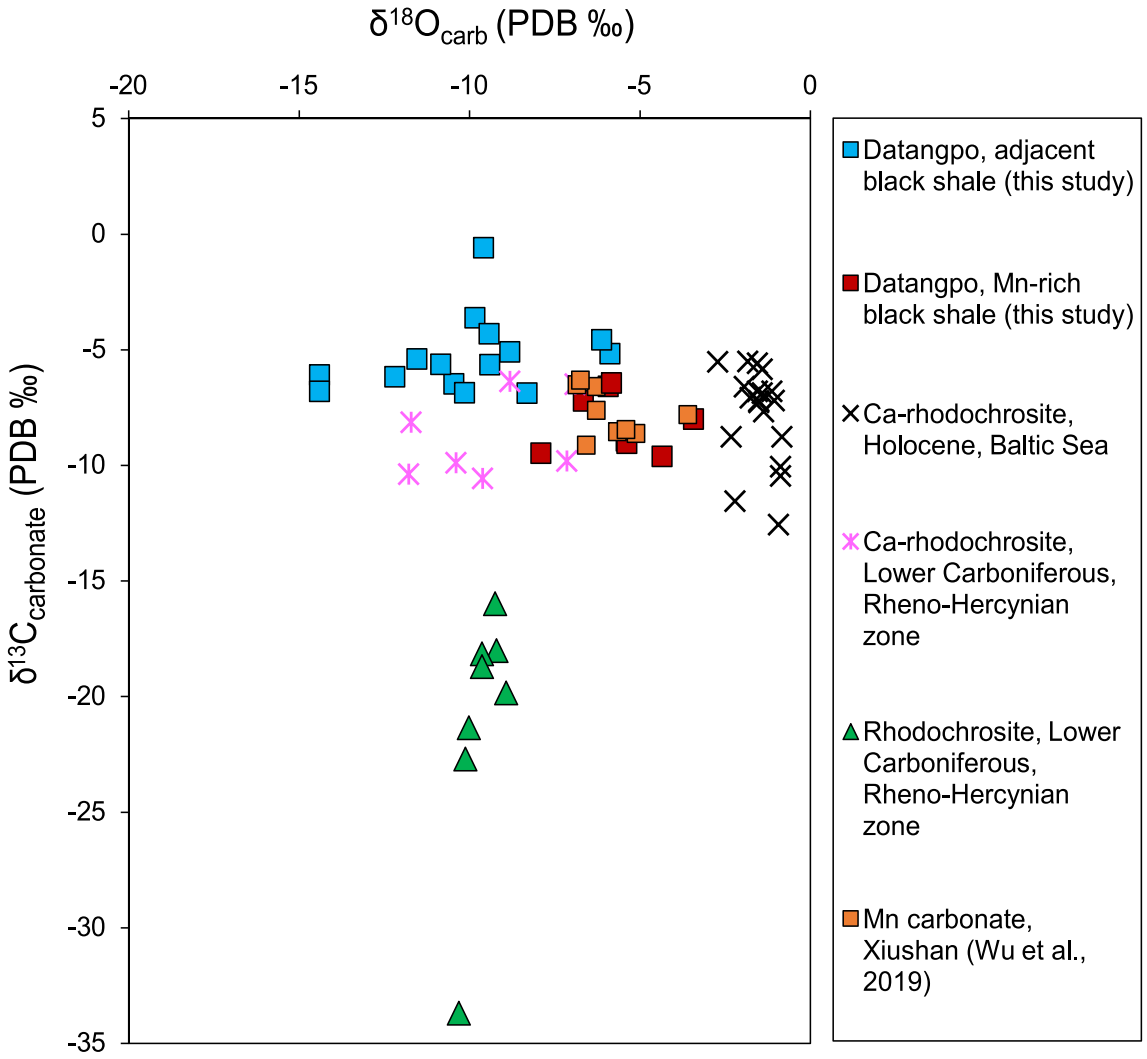

Fig. 7. Stable carbon and oxygen isotope data for the Mn-rich samples and the adjacent black shales from the lower member of the Datangpo Formation in South China. The literature data of Ca-rhodochrosite and rhodochrosite from the Holocene, Baltic Sea and Lower Carboniferous Rheno-Hercynian zone are from Huckriede and Meischner (1996). Mn carbonate data from the Xiushan section, South China are from Wu et al. (2016).

Both of these two abiotic (chemical) and biotic (microbial) mechanisms might have contributed to the formation of the Mn-carbonate bearing sediments in the Cryogenian Datangpo Formation in South China.

Positive Ce anomalies (Ce/Ce*), which are positively correlated with Mn (Fig. 6b), have been observed in most of the Mn-rich samples, but are absent in the adjacent black shales with low Mn contents (Fig. 6a). Ce has two valence states, the trivalent soluble form Ce(III), and the insoluble tetravalent form Ce(IV) (Maynard, 2010). Normalised Ce abundance relative to the neighbouring REEs can be used as a measurement of oxidative Ce removal. Due to the lower oxidative potential of Ce relative to Mn, oxidative scavenging of the soluble Ce(III) from seawater can be strongly controlled by Mn oxides (Brookins, 1988). In the oxygenated surface waters of the redox stratified Nanhua Basin, the positive Ce/Ce* could be due to absorption of pre-oxidised Ce on the surfaces of Mn oxide colloids, which then may be incorporated into Mn carbonates during diagenesis in the sediments (Sholkovitz et al., 1994). Ohnuki et al. (2008) and Tanaka et al. (2010) observed in lab experiments that Ce(III) was accumulated by Mn-oxidising bacteria, and was subsequently oxidised to Ce(IV) by biogenic manganese oxides. The microbial oxidation of Ce(III) to Ce(IV) on Mn oxide surfaces is a detoxification process operated by Mn-oxidising bacteria (Polgári and Gyollai, 2021). Therefore, the positive Ce/Ce* anomaly may have developed during the initial Mn precipitation process in the form of Mn oxide/hydroxide. The sequestration of Ce into the Mn-rich shales might have left the remaining seawater depleted in Ce, resulting in the absence of positive Ce anomalies in overlying and adjacent black shales. The positive Ce/Ce* values in the DTP-1 Mn-rich black shales are also consistent with the increasing spread in Ce/Ce* of Mn ores through geological time (Fig. 8). This could be the result of the increasingly oxidised state of the Cryogenian interglacial surface ocean and a progressively more diverse biosphere (Maynard, 2010).

The proposed initial Mn precipitation in the form of Mn oxide/hydroxide is further supported by their strong tendency to absorb certain transition metals, particularly Co, Mo, Ni, Zn and Pb (Maynard, 2010) (Fig. S1). Extensive studies of Co, Sr and particulate Mn in various redox stratified settings indicate intimate coupling of Mn and Co and/or Sr through adsorption or incorporation of Co by particulate Mn oxides in the oxic zone (Taillefert and Gaillard, 2002; Ivanets et al., 2017).

However, it is intriguing to note that the Mn-rich sample XS-21, which is petrographically characterised by Type II Mn carbonate, neither has a positive Ce anomaly (Ce/Ce* = 0.98) (Fig. 6 and Fig. 8; Table S1), nor has apparent enrichment of transition elements (Fig. S1).

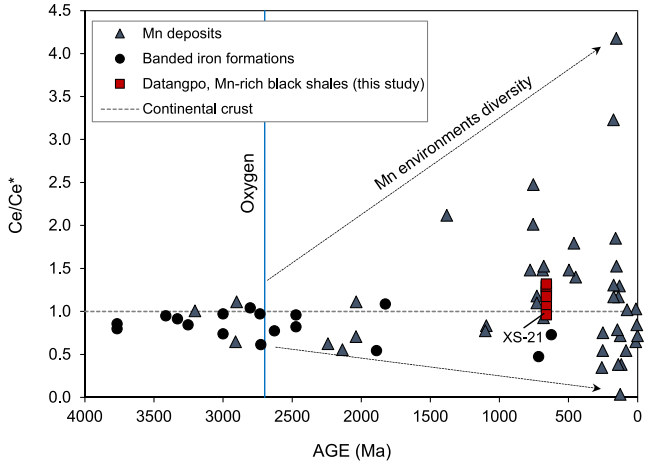

Fig. 8. Ce/Ce* for Mn deposits with age, modified from Maynard (2010). The diagram shows an increasingly spread trend through geological time, compared to the oxide-facies in the banded iron formations. The positive Ce/Ce* values of the Mn-rich black shales from the lower member of the Datangpo Formation are consistent with previously reported Late Neoproterozoic Ce/Ce* data (Maynard, 2010).

A terrestrial component derived from chemical weathering of the provenance, including quartz, feldspar, and pedogenic clay minerals mainly composed of illite, comprises the matrix of the Mn-rich shales (Ai et al., 2020b). A higher proportion of this terrestrial component in the Mn-rich samples with a relatively lower Mn carbonate content might have lowered the Ce/Ce* values to some extent. However, the Mn-rich samples with similar (e.g., XS-14 and XS-15) or even lower Mn content (e.g., MK-4) compared with XS-21 also have positive Ce anomalies (Fig. 6a; Table 1). In contrast, there are similarities between the Ce/Ce* values of Mn-rich samples characterised by Type II Mn carbonate (e.g., XS-21) and adjacent normal black shales with Mn content typically <0.1 wt% (Fig. 6a; Table 1). Such a distribution of Ce anomalies cannot be explained by a possible terrestrial effect. Therefore, the absence of positive Ce anomalies is very likely indicating a different initial precipitation phase for the Type II Mn carbonate.

Experimental studies on Mn-carbonate formation in the redox-stratified Brownie Lake in Minnesota, USA demonstrated that the introduction of calcite to Mn-rich waters at the chemocline can trigger substantial increases in rhodochrosite saturation due to the higher solubility of calcite compared with rhodochrosite (Wittkop et al., 2020). In the DTP-1 Mn-rich sample XS-21, the minor Ca-carbonate relics observed in the core of the Type II Mn-carbonate grains (Fig. 4c and 4d) likely indicate that the initial precipitation phase was $CaCO_3$, which later underwent partial to complete dissolution when it was in contact with more acidic water near and under the chemocline. The bubble structure that predominantly developed in the core phase is likely attributed to the release of CO_2 from the system during the precipitation of $CaCO_3$ ($Ca^{2+} + 2HCO_3^- \rightarrow CaCO_3 + CO_2 + H_2O$) (Dupraz et al., 2009). The dissolved Ca-carbonate relics might have acted as a nucleation site for rhodochrosite formation in the water column when Mn-supersaturation was reached, producing the rhomb-shaped authigenic $MnCO_3$ micro-crystals (Fig. 2e and 2f) (Siahi et al., 2020; Wittkop et al., 2020; Gao et al., 2021; Huang et al., 2022).

In addition to the availability of free Ca, carbonate precipitation is also a function of carbonate alkalinity. The glacial melt water might have supplied substantial alkalinity derived from the rapid carbonate weathering following the Sturtian glaciation, resulting in the formation of cap carbonates in the shallow water environment of the Nanhua Basin (Yu et al., 2020; Yu et al., 2022). However, this is likely not applicable for the delayed precipitation of the Type II Mn carbonate in the relatively deeper-water section of the Nanhua Basin during the peak of organic-rich black shale formation after the glaciation. It has been suggested that abiotic carbonate precipitation (e.g., calcite) could not have occurred under the extremely high pCO_2 levels (0.12 bars) at the early stage of Sturtian deglaciation, because of the high albedo effect of sea ice cover, until massive amounts of carbonate alkalinity reached the critical level to balance the high carbonic acid content of surface waters (Hoffman and Schrag, 2002; Kasemann et al., 2005; Shields, 2005; Ning et al., 2021). Considerable consumption of atmospheric CO_2 through intense chemical weathering after glaciation was likely to have buffered the seawater pH, changing it to a more alkaline condition (Kasemann et al., 2005; Wang et al., 2020; Ning et al., 2021). In addition, microalgae and cyanobacteria can also have a strong impact on the carbonate alkalinity of their surrounding environment by removing CO_2 through photosynthetic carbon fixation, resulting in alkalinity that favours $CaCO_3$ precipitation by disassociation of bicarbonate into CO_2 and OH^-. The elevation of marine primary productivity fuelled by increasing riverine nutrient input after glaciation, especially the blooming of cyanobacteria, might have facilitated Ca carbonate (e.g., calcite) precipitation by increasing the alkalinity of surface oxic water and providing mineral nucleation sites (i.e., whiting events) (Thompson et al., 1997; Dupraz et al., 2009; Herndon et al., 2018; Ai et al., 2021). Furthermore, anaerobic bacterial sulfate reduction could have made a supplementary contribution to the increase in alkalinity, and therefore the oversaturation of $MnCO_3$, by adding 2 mol of HCO_3^- for each mole of SO_4^{2-} consumed, despite the relatively low concentrations of sulfate in

Precambrian seawater (Baumgartner et al., 2006; Canfield and Farquhar, 2009; Algeo et al., 2015; Wittkop et al., 2020). Consequently, the authigenic precipitation of Ca-carbonate and its subsequent dissolution at the chemocline could have ultimately promoted the capture of Mn^{2+} by carbonate phases, driving the removal of residual Mn^{2+} and the initial precipitation of Mn as $MnCO_3$ in the water column. In essence, for the Type II Mn carbonate the initial incorporation of Mn^{2+} by Ca-carbonate relics is a physiochemically-forced precipitation pathway that operated in the water column, regardless of the presence of bacterial cells. The capture of Mn by carbonate phases may have precluded large-scale oxide precipitation if the rate of carbonate capture and burial equalled or exceeded the rate of Mn supply to the basin. Therefore, such *syn*-depositional precipitation of the Type II Mn carbonate likely happened at a later stage when pCO_2 and seawater Mn^{2+} supply rate decreased to the specific level that is suitable for authigenic carbonate formation. Enhanced aerobic decomposition of organic matter derived from elevated marine primary production at this time might have lowered the O_2 concentration in surface waters to a level that is not sufficient to support microbially-mediated Mn oxidation.

5.2. The multiple roles of organic matter (living and nonliving) in the formation of Mn carbonate

5.2.1. Microbial-influenced oxidation and reduction of Mn

As discussed above, most of the DTP-1 Mn-carbonate ores are inferred to initially have been precipitated as Mn oxides, which are likely the precursors of the Type I Mn carbonate. Unlike other redox-sensitive transition metals (e.g., Fe) which can be oxidised under anoxic conditions with alternative oxidants such as nitrate, Mn is rather unique in its environmental specificity for O_2 as an electron acceptor (Konhauser et al., 2002; Clement et al., 2009; Smith, 2015). However, the formation of Mn oxide/hydroxide, as a precursor of Mn carbonate that formed later in organic-rich sediments, requires a high redox potential (i.e., higher Eh values) (Diem and Stumm, 1984; Tebo et al., 2004; Rajabzadeh et al., 2017). It is generally considered that Mn is not able to precipitate from sterile solutions lacking catalysis associated with microbes, even in the presence of relatively high abundances of free oxygen (Tebo et al., 2004; Stumm and Morgan, 1995; Morgan, 2005; Smith and Beukes, 2023). A fundamental problem with the Cryogenian DTP-1 Mn deposits in South China is that there was not sufficient O_2 flux in the redox-stratified Nanhua Basin to support the observed quantity of Mn oxide formation (Cheng et al., 2018; Ye et al., 2018). Microbially-mediated Mn oxidising processes are very effective when compared with chemical processes (up to 10^5–10^6 times more effective), and generally produce minerals of very fine-grained (μm scale) texture (Tebo et al., 1997; Polgári and Gyollai, 2021). In sedimentary environments, Mn(II) oxidation is facilitated by enzymatic reactions involving multi-copper oxidase enzymes in a diverse array of bacteria (Tebo et al., 2004; Webb et al., 2005; Sutherland et al., 2018). Such catalytic oxidation reactions have been observed on bacterial spores (Rosson and Nealson, 1982) and in association with extracellular polymeric substance (EPS), which is an extension of microbial cells and is most likely produced by cyanobacteria (Dupraz et al., 2009). The bacterial origin of organic matter of the Cryogenian interglacial strata, especially the bloom of cyanobacteria, might have played a key role in regulating the Mn oxidation that occurred in surface seawater in the Nanhua Basin (Brocks et al., 2017; Ai et al., 2020a).

It has been suggested that high Mn^{2+} concentrations in pore water as a result of *in-situ* reduction of Mn(IV) oxide precursors is the prerequisite for diagenetic Mn-carbonate formation (Calvert and Pedersen, 1996; Johnson et al., 2016; Häusler et al., 2018). The reduction of Mn oxides generally occurs at a shallow depth (~10 cm) beneath the sediment–-water interface, and is commonly regulated by dissimilatory metal-reducing microbes (Van Cappellen et al., 1998). During this process, organic matter could have served as an electron donor (see details in Section 5.2.3) (Nealson and Saffarini, 1994; Van Cappellen et al., 1998; Johnson et al., 2016; Biondi and Lopez, 2017).

5.2.2. Transfer of the Mn-bearing mineral grains to the sediments

In the aftermath of the Sturtian glaciation, the elevated sulfate concentration in seawater derived from rapid oxidative weathering of continental sulfides triggered the development of metastable euxinic conditions in the context of extensive anoxic deep waters (Ye et al., 2018). Based on the inferred oceanic water conditions in the Cryogenian interglacial Nanhua Basin, the Type I Mn-rich ores were mainly developed under suboxic-anoxic conditions during temporary ocean oxygenation in the aftermath of the Sturtian glaciation (Lau et al., 2017; Ai et al., 2021). The Mn-rich sample XS-21 contains Type II Mn carbonate, and was deposited during the subsequent stable euxinic stage (Li et al., 2012; Ai et al., 2021).

Reductive dissolution of Mn(IV) oxides is expected to have occurred rapidly below the chemocline due to high concentrations of sulfide and dissolved Fe^{2+} reductants (Myers and Nealson, 1988). However, an essential link between the initial precipitation of Mn as oxides in surface seawater and the subsequent reduction of Mn oxides in sediments has long been neglected: when settling through the anoxic deep waters, how the Mn(IV) oxides eventually reached the sediments on the seafloor before being reductively dissolved. Humus, a microbial decomposition product of organic matter with a colloidal structure, has multiple functional groups (e.g. —COOH) and a strong absorption capacity. It has been shown that humus colloid is able to trap and transport a diverse array of metal minerals through anoxic/euxinic deep waters, promoting their precipitation during early diagenesis at the sediment–water interface (Suess, 1979). In addition, EPS also has unique gel-like properties that provide a substrate for coagulation of the authigenic metal minerals (e.g., Mn oxides, calcite) that are formed in the water column. In environments where there was recovery of marine primary production during deposition of the post-glacial DTP-1 formation, substantial increases of organic matter input and therefore widely distributed humus and/or EPS in water column would be expected. The abundant organic matrix that is distributed as a cement around the Type I Mn-carbonate grains very likely represents residual humus and/or EPS (Fig. 3a, 3b and 3f). For the Type II Mn carbonate, the physiochemically-forced initial incorporation of Mn^{2+} by Ca-carbonate relics, and thus the formation of the Mn-rich shells, might have protected Mn-Ca carbonate grains from further dissolution as they settled through the prevailing euxinic bottom waters in the Nanhua Basin (Herndon et al., 2018; Wittkop et al., 2020). However, the role of humus and/or EPS for transporting the Type II Mn carbonate cluster cannot be excluded (Fig. 4). The bathtub ring model (Roy, 2006; Yu et al., 2016), which also involves preformed Mn oxides and subsequent formation of Mn carbonate during diagenesis, is not applicable for the Datangpo Formation Mn deposits in South China. This is because the Datangpo Formation Mn deposits are principally found in the deep subbasins of the Nanhua Basin, rather than around the subbasin margins, as characterized by the bathtub ring pattern (Roy, 2006; Yu et al., 2016).

5.2.3. Predominant carbon source for Mn-carbonate formation

The carbon in Mn-rich carbonates might have originated from seawater bicarbonate ($\delta^{13}C = \sim 0$ ‰), bicarbonate derived from oxidised organic matter in sediments ($\delta^{13}C = -20$ ‰ to -30 ‰), or may have been produced by the anaerobic oxidation of methane ($\delta^{13}C = -40$ ‰), or combinations of these sources and processes (Okita et al., 1988; Cavagna et al., 1999; Roy, 2006; Zhou et al., 2013; Maynard, 2014). Mn-carbonates formed through reactions involving organic carbon during early diagenesis are depleted in ^{13}C (Okita and Shanks, 1992; Fan et al., 1999). For example, Polgári et al. (2012a) proposed a microbial contribution to the rhodochrosite in the Úrkút Mn deposit in Hungary, based on the low $\delta^{13}C_{carb}$ values (~−16.8 ‰). The ^{13}C depleted ($\delta^{13}C_{carb} = -12.2$ ‰ to -21.3 ‰) Mn carbonate-bearing mudstones in the Mesoarchaean Witwatersrand-Mozaan succession of southern Africa also support a contribution from organic carbon during microbial-

mediated precipitation of Mn carbonate (Smith et al., 2023).

For the Mn-rich samples containing Type I Mn carbonate, the negative $\delta^{13}C_{carb}$ values (−7.2 ‰ to −9.6 ‰, average = −8.7 ‰) likely points to a contribution of dissolved inorganic carbon from oxidised organic matter (humus colloid and/or EPS) after burial in the anoxic sediments (Fig. 7; Table 1) (Okita et al., 1988; Veizer et al., 1989; Maynard, 2010). During this process, the "trapped" Mn oxides would have been degraded through anaerobic metabolisms, giving rise to significantly elevated interstitial concentrations of HCO_3^- and Mn^{2+} to the extent that exceeded their saturation limits, eventually resulting in precipitation of mixed valence Mn-carbonates including rhodochrosite and Ca-rhodochrosite (Suess, 1979; Calvert and Pedersen, 1996; Thamdrup et al., 2000; Learman et al., 2011; Polgári et al., 2012b). The Mn-rich samples that contain predominantly Type II Mn carbonate (e.g., sample XS-21) contain relatively less negative $\delta^{13}C_{carb}$ (about −6.5 ‰) than the samples that are characterised by Type I Mn carbonate (e.g., sample MK-2) with an average $\delta^{13}C_{carb}$ of −8.7 ‰ (Fig. 7; Table 1). This indicates that HCO_3^- derived from dissolved Ca carbonate (e.g., calcite) that precipitated in oxic surface waters is likely to have made more contributions to the Mn-rich samples with Type II Mn carbonate (Herndon et al., 2018). However, a contribution of HCO_3^- from organic matter during the growth of the Type II Mn carbonate in the water column or after burial cannot be excluded. Due to the significantly low $\delta^{13}C_{org}$ of about −35 ‰ for organic carbon derived from cyanobacteria and possible algae in the Datangpo Formation (Ai et al., 2021), any contribution of HCO_3^- from organic matter might have caused the $\delta^{13}C_{carb}$ of Mn-rich samples with Type II Mn carbonate to be lower than the typical Cryogenian seawater $\delta^{13}C$ of −2 ‰ to +2 ‰ (Yu et al., 2017). Thus, petrographic observation is essential for distinguishing the Type II Mn carbonate.

Recent studies revealed that Mn-rich and ^{13}C-depleted carbonates can also be derived from the anaerobic oxidation of methane by Mn oxides in sulfate-poor environments such as the Precambrian ocean (Cai et al., 2021). Nevertheless, this geochemical process is unlikely to have made a significant contribution to the ^{13}C-depleted DTP-1 Mn carbonates in South China, due to the dissimilarity of the $\delta^{13}C_{carb}$ of the DTP-1 Mn carbonates to the extremely low $\delta^{13}C$ values of biogenic methane (<−50 ‰) (Whiticar, 1999). The Mn carbonate formed through thermochemical Mn oxide reduction by thermogenic methane at temperatures >95 °C have $\delta^{13}C$ values of heavier than −10 ‰ (Beal et al., 2009; Hu et al., 2018; Cai et al., 2021), similar to those of the DTP-1 Mn carbonates. However, the DTP-1 Mn carbonates formed during early diagenesis (Type I) or directly from the water column (Type II), at which stage the organic matter was far from thermally mature, and thus could not have generated oil or gas, including methane, by thermal cracking.

The detection of mainly small organic fragments in the ToF-SIMS negative spectra is typical for a ToF-SIMS signal from a macromolecular organic structure that was produced by high thermal maturity. It has been shown that the Type I Mn carbonates are closely localised in the organic matter enriched phase (Fig. 5). The patchy spatial distribution of these organic fragments is consistent with the distribution of the organic matter, which is mostly found in the growth zones of the Type I Mn carbonates. This straightforwardly reveals the consanguinity of the carbon in the Mn-rich carbonates and the carbon derived from organic matter. In addition, the predominant CN^- distribution in the ToF-SIMS data (Fig. 5) is consistent with the high thermal maturity of the Mn-rich samples, which have an equivalent vitrinite reflectance of ~2.5 % (Ai et al., 2020a). At such an over-mature stage, high molecular weight cyclic biomarkers (organism-specific organic molecules) have almost completely been converted into other compounds, primarily aromatic macromolecules.

Dupraz et al. (2009) suggested that bacterial cells and/or their EPS can be passively or actively incorporated within the carbonate mineral product, where they serve as physical substrates for carbonate precipitation. In the Type I Mn carbonate grains, the distribution of the organic-rich ring that follows the concentric laminae (Fig. 3b and 3c) also suggests that the incorporation of organic matter occurred during the accretion processes, which is consistent with the former presence of microbial biofilms, for example the residues of EPS biofilms. In addition, the cavities observed in the organic ring, whose sizes and shapes are similar to single cells (Fig. 3b and 3c), may represent entrapped remnants of the Mn-reducing bacteria that heterotrophically reduced Mn oxides at the expense of organic matter as an electron donor (Zhang et al., 2015b; Huang et al., 2022). However, the organic ring and the cell-like cavities are not present in the Type II Mn carbonates (Fig. 4), further supporting a predominantly inorganic source of carbon derived from the dissolved Ca-carbonate.

5.2.4. *The formation of the ooidal-like structures in the Mn-carbonate grains*

Several studies of the interglacial DTP-1 Mn carbonates in South China have addressed the role of microorganisms in regulating the reduction of pre-formed Mn oxides and providing a carbon source, but the micrometre-scale ooidal texture of the DTP-1 Mn carbonates has seldom been reported, and its nucleation pathway is poorly constrained. Organo-mineralisation experiments using bacterial cells or EPS have shown that polymer properties, for example water content and abundant acidic functional groups, can greatly influence the morphology and mineralogical characteristics of carbonate minerals by regulating the saturation of the binding capacity for particular metal ions (Costerton et al., 1995; DeFarge et al., 1996; Rodriguez-Navarro et al., 2007; Dupraz et al., 2009).

In addition to influencing the mm-scale properties of minerals, the EPS can also affect the nano-scale structure of carbonate precipitates. The growth banding of the ooidal Mn carbonates that formed under suboxic/anoxic conditions reflect the formation of different stoichiometry carbonates in response to variations of the $[Mn^{2+}]$:$[Ca^{2+}]$ ratio in solution during decay of EPS (Costerton et al., 1995; Mucci, 2004). The Ca-rich rhodochrosite often undergoes carbonate diagenesis to generate the rhodochrosite endmember ($MnCO_3$) (Johnson et al., 2016). The Ca^{2+} released during this process can form authigenic gypsum when it encounters high concentrations of SO_4^{2-} in porewater (Fig. 2c), which can be supplied by diffusion from seawater or by oxidation of previously-formed reduced sulfur species (e.g., HS^-) during biologically-mediated reduction of Mn(IV) oxides (Aller and Rude, 1988; Henkel et al., 2019; Liu et al., 2018). The μm-scale gypsum crystals with radial, fibrous flower-like structures in the fresh shales are very unlikely to have been formed during weathering, drilling or sample storage, because the outer layers of the samples were cut off before analysis. In addition, these gypsum crystals are only present in the Mn-rich samples characterized by the Type I Mn carbonate, and are absent in other samples with even higher content of pyrite. The precipitation of $MnCO_3$ would lower the $[Mn^{2+}]$:$[Ca^{2+}]$ ratio in solution, promoting the formation of the outer Ca-rich Mn carbonate layer (e.g. Ca-rhodochrosite or kutnohorite), which represents a new cycle of growth (Fig. 3b, 3c and 3e). Such a growth pattern is consistent with the paragenetic model of Mn mineral phases that was proposed by Johnson et al. (2016). This is a relatively slow diagenetic process, explaining the comparatively larger grain size of 2–5 μm for the Type I Mn carbonates.

Unlike the ooidal-like structure of the Type I Mn-carbonate grains, the newly identified Type II Mn carbonate in this study has a core–shell structure with a minor Ca-carbonate core (likely to be calcite) enclosed by a rhodochrosite shell (Fig. 4). The smaller grain size (<2 μm) of the Type II Mn carbonates might be due to the quick physiochemical nucleation of oversaturated Mn^{2+} and HCO_3^- in the water column (Polgári and Gyollai, 2021). The small grain size and the simple core–shell structure of the Type II Mn carbonates would likely be preserved after burial, due to limited diffusion-based crystal growth because of the diminished seawater Mn concentration, caused by substantial precipitation of Mn ores dominated by the ooidal Type I Mn carbonates during the early stage of deglaciation.

5.3. The post-depositional (Type I) versus syn-depositional (Type II) formation pathways of the ooidal-like Datangpo formation sedimentary Mn carbonates

Based on the discussions above, two distinct formation pathways of the ooidal-like DTP-1 Mn carbonate hosted in black shales are proposed here.

The metallogenesis of the Cryogenian interglacial Type I Mn carbonate in South China is likely to have been a consequence of multiple reactions involving Mn oxidation and reduction via microbially-mediated diagenetic processes (Fig. 9A). During the Sturtian glaciation, hydrothermally-derived Mn(II) accumulated in the anoxic deep waters under ice cover (Roy, 2006). Convection of the ocean was reinitiated by the Sturtian deglaciation, bringing the stored Mn(II) and nutrient-rich deep waters to the surface layer by upwelling (Wu et al., 2016; Yu et al., 2016). This stimulated the recovery of marine primary productivity, predominantly by cyanobacteria (Brocks et al., 2017), and led to the development of redox-stratification (Fig. 9A) (Li et al., 2012). The Mn(II) that accumulated in the well-oxygenated surface waters was oxidised to form particulate Mn oxide/hydroxide through processes mediated by Mn-oxidising bacteria (Fig. 9A). These Mn oxide/hydroxide particles were subsequently trapped, nucleated and transported to deep

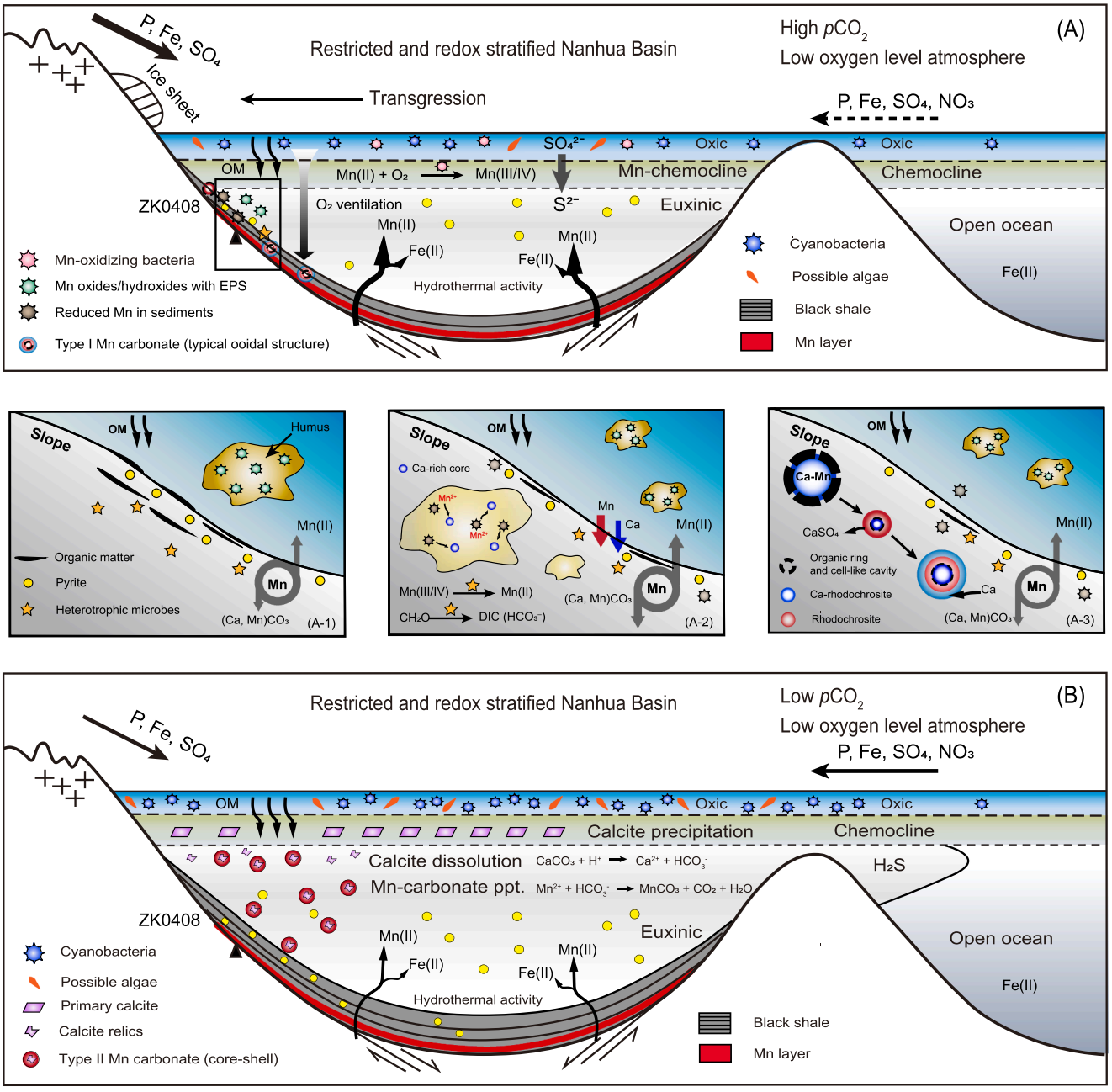

Fig. 9. Formation model for the two distinct types of ooidal Mn carbonates hosted in the black shales from the Cryogenian interglacial lower member of the Datangpo Formation in South China. (A) Macro-scale sedimentary model, showing the post-depositional pathway for the Type I Mn-carbonate during the early stage of Sturtian deglaciation. The Type I Mn-carbonate is a microbially-mediated metallogenesis product, during which process the organic matter played multiple roles, including catalysing Mn redox cycling, transporting pre-formed Mn oxides, and serving as a carbon source. (A-1) (A-2) (A-3) Enlarged figures of the marked rectangle in (a), showing the sequential formation of growth banding in the Type I Mn-carbonate ooids. OM = Organic matter. (B) Syn-depositional model for the Type II Mn-carbonate, showing its physiochemically-forced formation pathway. The relics of the primarily precipitated Ca-carbonate (e.g., calcite) served as the nucleation seeds for Mn-rich carbonate precipitation. ppt = precipitation.

waters by humus and/or EPS biofilms (Fig. 9A-1). The pulsed oxygen ventilation events triggered by mass gravity flows at the slope section facilitated the accumulation of the pre-formed Mn oxides colloids in the organic-rich sediments (Clement et al., 2009; Yu et al., 2016). During decomposition of the wrapped organic matter (i.e., organic matrix and/or EPS), the Mn oxides are inferred to have been reduced to soluble Mn (II) through processes mediated by heterotrophic microbes under suboxic-anoxic conditions (Fig. 9A-2). The release rate of Mn(II) and EPS-bound metal ions (e.g., Ca^{2+} and Mg^{2+}) to porewater is largely regulated by the efficiency of heterotrophic reactions (Mucci, 2004; Maynard, 2014). Local increases in alkalinity favoured the precipitation of Ca-rich microspheres, which can act as seeds for further crystallisation and concentric growth of solid solution Mn-Ca-carbonate (e.g. Ca-rhodochrosite and kutnahorite, $CaMn(CO_3)_2$) and $MnCO_3$ rings, which resulted in the development of the ooidal-like texture of the Type I Mn-carbonate grains (Fig. 9A-3) (Mucci, 2004; Aloisi et al., 2006). In summary, formation of the Type I Mn carbonate was a post-depositional diagenetic event, during which process the organic matter, including living microbes and sedimentary organic matter, played multiple functions.

In contrast, formation of the Type II Mn carbonate was predominantly a physiochemically-forced *syn*-depositional pathway, during which process the Mn carbonate developed from primary Ca-carbonate (e.g., calcite) crystals precipitated under lowered pCO_2, as a consequence of intense chemical weathering in the aftermath of the Sturtian glaciation (Fig. 9B). Supersaturation of Mn carbonate is enhanced when Ca-carbonate originating from surface waters dissolves in more acidic waters at the chemocline. The Ca-carbonate relics served as nucleation seeds for further growth of the Mn-rich carbonate crystals. Instead of representing diagenetic organic carbon degradation in sediments, the negative carbon isotope composition of the Type II Mn carbonates was very likely imparted by dissolved calcite and by limited organic carbon remineralisation in the water column. This study supports the hypothesis that primary Mn-carbonates can originate from waters containing 5 μM dissolved O_2 or less, and do not require the burial of precursor Mn-oxides in sediments (Wittkop et al., 2020).

5.4. Implications for the Cryogenian carbon cycle

The DTP-1 Mn-rich carbonate deposit is an important link in the carbon cycle of the transitional Neoproterozoic Era, as the formation mechanism was controlled mainly by the specific geochemical composition of the atmospheric-oceanic system. In turn, massive metallogenesis of Mn in the black shale-hosted carbonate phase may have had a potential impact on the Neoproterozoic carbon cycle by regulating the chemical composition of the surface Earth environment. Burial of organic matter can be a net sink of CO_2, and its mineralisation can result in the production of greenhouse gasses such as methane and CO_2 (Keil, 2011). The bulk of the organic carbon lost during early diagenesis is mainly due to sulfate reduction ($2CH_2O + SO_4^{2-} \rightarrow H_2S + 2HCO_3^-$) (Berner, 1989; Friese et al., 2021). But in the case of the massive Mn-rich sediments deposited in the sulfate-poor Precambrian seawater, the microbially-mediated formation of Mn carbonates by reduction of Mn oxides played a significant role in consuming organic carbon ($CH_2O + MnO_2 \rightarrow Mn^{2+} + HCO_3^-$). For the Mn-rich Datangpo Formation samples from multiple sections across South China, a trend of decreasing TOC in response to increasing Mn content can be recognised (Fig. 10a). Similar diagenetic consumption of organic carbon might also have operated in some of the Precambrian iron formations, resulting in their depleted organic carbon content coupled with negative $\delta^{13}C_{carb}$ composition (Klein, 2005; Heimann et al., 2010; Smith et al., 2013). Although Mn-carbonate formation during early diagenesis is not favourable for organic carbon preservation, sedimentary Mn carbonate deposition at a notable scale may prevent the CO_2 produced by aerobic oxidation of organic carbon diffusing back to the surface system, providing an additional contribution for atmospheric CO_2 drawdown and thus increasing the pO_2/pCO_2 ratio (Roy, 2006). Massive Mn carbonate formation can thus be regarded as a special microbial carbon pump, which converts burial/dissolved organic carbon to recalcitrant/inactive inorganic carbon (Fig. 11a). The storage of inorganic carbon by Mn carbonates over geological time can potentially regulate climatic conditions, chemical weathering intensity, and atmospheric-oceanic oxygen levels.

It is intriguing to notice that the enrichment of phosphorous (P_{EF}) consistently coincides with higher Mn content for multiple sections in South China (Fig. 10b). It has been suggested that the association of phosphorous with particulate Mn can occur during the initial massive precipitation of MnO_x during pulsed oxygenation events, probably linked to injection of O_2-laden surface waters (Jilbert and Slomp, 2013). During the subsequent conversion of Mn oxides emplaced in organic-rich sediments to (Ca-)rhodochrosite, the phosphorous might have substituted for carbonate in the rhodochrosite structure, generating a mixed Mn-Ca-carbonate-phosphorous phase (Suess, 1979; Jilbert and Slomp, 2013). The fixation of phosphorous in authigenic Ca-Mn-

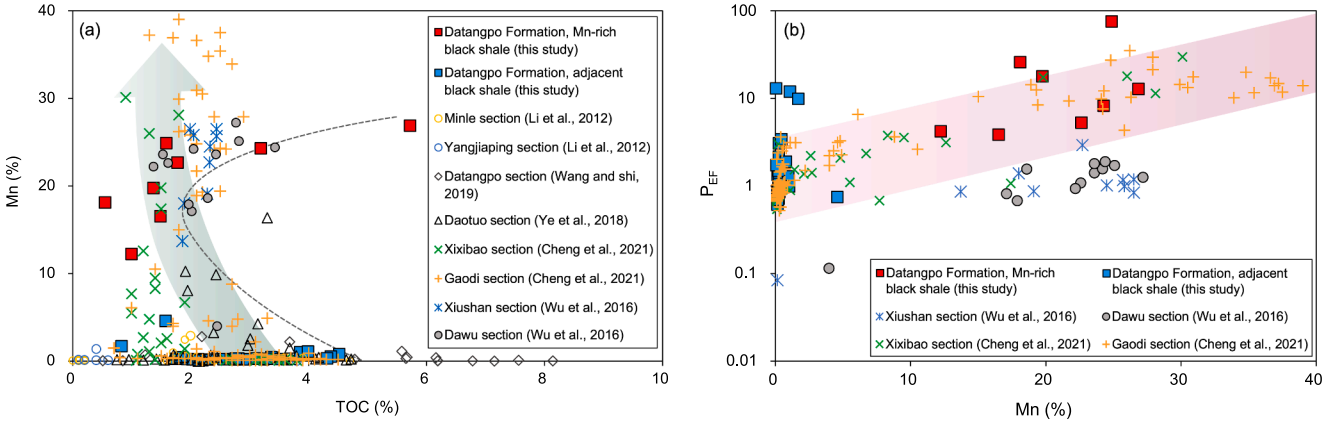

Fig. 10. (a) Cross plot of total organic carbon (TOC, wt%) versus Mn content (wt%). There is a general decreasing trend of TOC with increasing Mn content. Microbially-mediated Mn-carbonate formation at the expense of organic carbon during early diagenesis is not favourable for organic carbon preservation. (b) Cross plot of Mn content (wt%) versus the enrichment of phosphorous (P_{EF}). $P_{EF} = (P/Al)_{sample}/(P/Al)_{PAAS}$. A positive correlation between Mn and P_{EF} can be observed. Samples that deviate from the general trend may represent more contribution of Type II Mn-carbonate. Background data from multiple sections in South China are from the literature. Data on the Minle and Yangjiaping sections are from Li et al. (2012). Data on the Dawu and Xiushan sections are from Wu et al. (2016). Data on the Daotuo and Datangpo sections are from Ye et al. (2018) and Wang and Shi (2019), respectively. Data on the Xixibao and Gaodi sections are from Cheng et al. (2021).

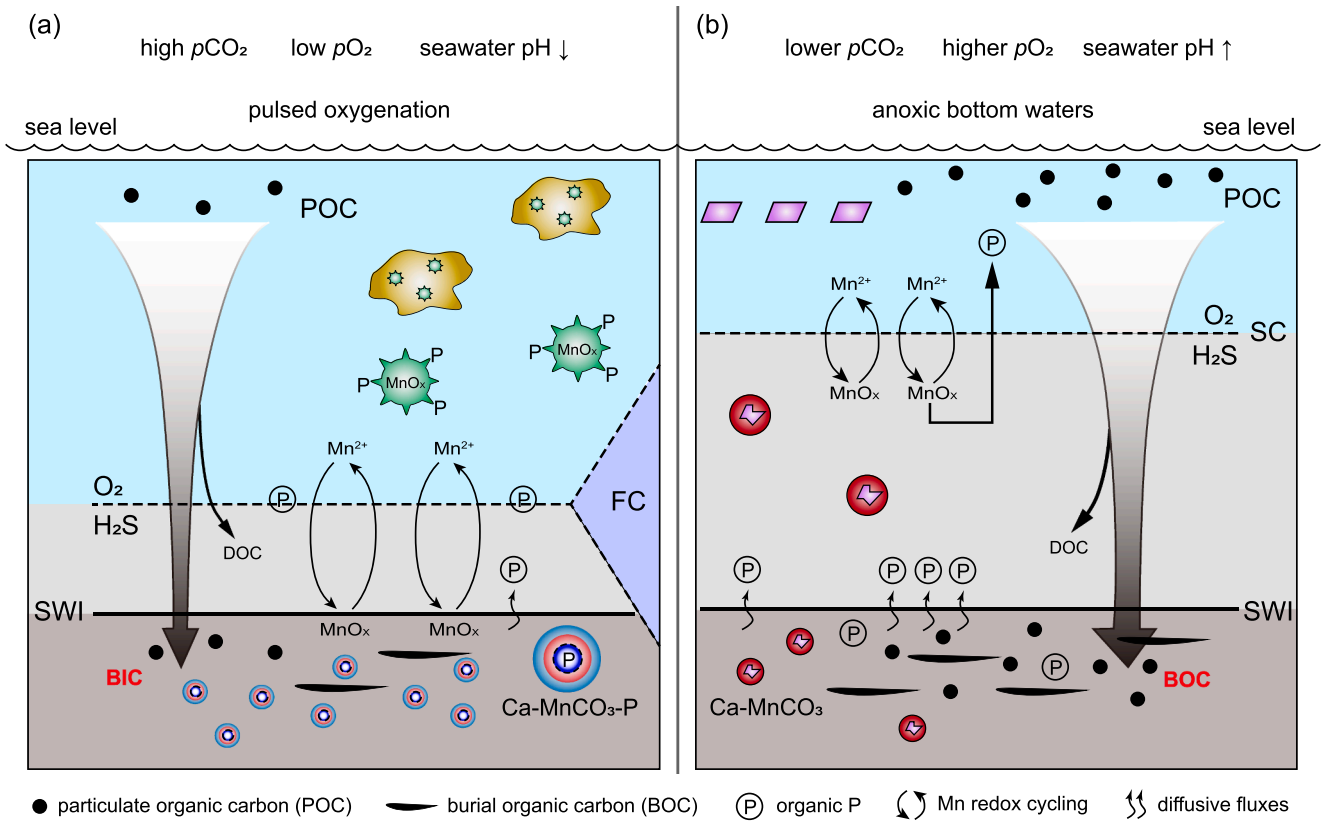

Fig. 11. Summary of the biological carbon pump and P cycling during formation of the black shale hosted (Ca-) Mn carbonate in the Cryogenian interglacial Datangpo Formation, South China. (a) Massive deposits of Type I Mn-carbonate formed through a microbially-mediated diagenetic pathway soon after the Sturtian glaciation, and converted organic carbon to buried inorganic carbon, preventing recycling of CO_2 derived from organic carbon respiration from diffusing back to the atmosphere. Less efficient regeneration of P due to authigenic Ca-$MnCO_3$-P precipitation via the MnO_X shuttle under pulsed oxygenation events probably constrained primary production and C_{org} burial, limiting the rapid accumulation of atmospheric O_2. (b) Authigenic formation of the Type II Mn-carbonate under a more reducing water column favoured the burial of C_{org} and higher primary production fuelled by efficient P cycling. For detailed explanation of the symbols see the legend of Fig. 9.

carbonate phases likely facilitated retention of phosphorous in the sediments. As the ultimate limiting nutrient for marine primary production, less efficient phosphorous recycling during the massive precipitation of the Type I Mn carbonates likely slackened recovery of marine primary production, and therefore impeded rapid accumulation of O_2 in the paleo-ocean and atmosphere after the Sturtian glaciation (Fig. 11a) (Guilbaud et al., 2020). In contrast, the Type II Mn carbonates precipitated directly from the water column, which does not support authigenic sequestration of phosphorous into mineral phases (Fig. 11b). The data points that deviate from the positive correlation of Mn and P_{EF} may represents more contribution of Type II Mn carbonates to these Mn-rich samples under more reducing conditions (Fig. 10).

6. Conclusions

By systematically revisiting the petrographic and geochemical characteristics of the post-Sturtian Datangpo Formation in South China, this study has demonstrated the coexistence of two distinct formation mechanisms for the black shale-hosted Mn carbonates with particular micro-ooidal structures. The Type I Mn carbonates are characterised by multiple cycles of growth banding, and are proposed to have formed through microbial-mediated Mn redox cycling under a relatively high pCO_2, coupled with density flow that could have injected the O_2-laden surface waters into sediments in the early stage of Sturtian deglaciation. In addition to serving as a redox-cycling catalyst, the negatively-charged functional groups in organic matter (i.e., humus and/or EPS biofilms) also facilitated the accumulation and transportation of precursor Mn oxides, by protecting them from being reductively dissolved before reaching the organic-rich sediments. The bacterial cells and/or their EPS were likely to have been passively or actively incorporated within the Mn-Ca carbonate mineral products when they served as physical and metabolism substrates for Mn carbonate precipitation during early diagenesis, leading to the formation of kerogenous laminae (i.e., the organic-rich rings) and cell-like cavities and the growth-banding in the ooids.

Importantly, novel evidence indicates that the capture of Mn as a carbonate phase directly from water column, referred to as the Type II Mn carbonates, might also have contributed to the formation of the Datangpo Formation Mn carbonate deposit. This mechanism became predominant under lowered pCO_2 and therefore buffered seawater alkalinity after intense chemical weathering during deglaciation. At this stage, the expansion of anoxic/euxinic condition was very likely a result of enhanced aerobic degradation of increased organic matter input, fuelled by terrestrially-derived nutrients. This indicates that *syn*-depositional precipitation of Mn carbonate can occur in more reducing environments than previously recognised. Rapid oversaturation of Mn carbonate in the water column led to the comparatively smaller grain size and relatively simple ooidal structure (i.e., core–shell structure) of the Type II Mn carbonates, in contrast with the Type I Mn carbonates. This study has shown that spherulitic or short-rod shapes, and the ooidal-like texture of the Mn-carbonate grains, do not necessarily indicate organomineralisation. The initial precipitation phase has to be carefully distinguished to conclusively determine a biotic or abiotic mineral origin. The identification of two coexisting and distinct formation mechanisms for Mn carbonates (i.e., post-depositional biotic pathway and *syn*-depositional abiotic pathway) provides a more nuanced logic for understanding the mineralogical and textural observations of the Mn-rich sedimentary rocks in South China. Importantly, it

is suggested that large-scale sedimentary Mn carbonate deposits served as a particular storage of inorganic carbon and a supplementary retention of phosphorous, which could have regulated primary production, C_{org} burial, climatic conditions, and the extent of atmospheric O_2 accumulation. This study sheds light on a more comprehensive understanding of biogeochemical carbon cycling and the co-evolution of eukaryotes on the Cryogenian Earth's surface environments.

CRediT authorship contribution statement

Jiayi Ai: Conceptualization, Investigation, Data curation, Validation, Visualization, Writing – original draft. **Sandra Siljeström:** Resources, Data curation, Validation, Visualization, Writing – original draft. **Ningning Zhong:** Project administration, Funding acquisition, Supervision, Resources, Validation, Writing – review & editing. **Jianfa Chen:** Funding acquisition, Validation, Writing – review & editing. **Tieguan Wang:** Validation, Writing – review & editing. **Nansheng Qiu:** Validation, Writing – review & editing. **Simon C. George:** Supervision, Funding acquisition, Writing – review & editing.

Declaration of Competing Interest

The authors declare that they have no known competing financial interests or personal relationships that could have appeared to influence the work reported in this paper.

Data availability

The authors do not have permission to share data.

Acknowledgements

This project was funded by the National Key Research and Development Program of China (2017YFC0603100). We thank the Chongqing Institute of Geology and Mineral Resources, and Yu Zhang and Lipeng Yao at the China University of Petroleum-Beijing for assistance in the field. Professor Ruizhong Hu at the Institute of Geochemistry (Chinese Academy of Sciences) in Guiyang is thanked for analysing the major and trace elements. Yanru Zhang at the China University of Petroleum-Beijing is thanked for producing the element distribution maps. Jiayi Ai was supported by China Postdoctoral Science Foundation (2022M713457), Science Foundation of China University of Petroleum-Beijing (No. 2462022XKBH004), and a Macquarie University Research Excellence Scholarship. Sandra Siljeström was funded by the Swedish Research Council (contract 2015-04129) and Swedish National Space Agency (contracts 198/15 and 137/19). We much appreciate the valuable comments from editor Dr. Frances Westall, reviewer Dr. Bertus Smith and one anonymous reviewer, which have much improved the content and structure of this manuscript.

Appendix A. Supplementary material

Supplementary figures, tables, and supporting materials on the origin of the manganese. Supplementary data to this article can be found online at https://doi.org/10.1016/j.precamres.2023.107091.

References

Ai, J., George, S., Zhong, N., 2020a. Organic geochemical characteristics of highly mature Late Neoproterozoic black shales from South China: Reappraisal of syngeneity and indigeneity of hydrocarbon biomarkers. Precambr. Res. 336, 105508.

Ai, J., Ningning, Z., George, S.C., Yu, Z., Lipeng, Y., Tieguan, W., 2020b. Evolution of paleo-weathering during the late Neoproterozoic in South China: Implications for paleoclimatic conditions and organic carbon burial. Palaeogeogr. Palaeoclimatol. Palaeoecol., 109843.

Ai, J., Zhong, N., Zhang, T., Zhang, Y., Wang, T., George, S.C., 2021. Oceanic water chemistry evolution and its implications for post-glacial black shale formation: Insights from the Cryogenian Datangpo Formation, South China. Chem. Geol. 566, 120083.

Algeo, T.J., Luo, G.M., Song, H.Y., Lyons, T.W., Canfield, D.E., 2015. Reconstruction of secular variation in seawater sulfate concentrations. Biogeosciences 12, 2131–2151.

Aller, R.C., Rude, P.D., 1988. Complete oxidation of solid phase sulfides by manganese and bacteria in anoxic marine sediments. Geochim. Cosmochim. Acta 52, 751–765.

Aloisi, G., Gloter, A., Krüger, M., Wallmann, K., Guyot, F., Zuddas, P., 2006. Nucleation of calcium carbonate on bacterial nanoglobules. Geology 34, 1017–1020.

Barley, M., Groves, D., 1992. Supercontinent cycles and the distribution of metal deposits through time. Geology 20, 291–294.

Bau, M., Dulski, P., 1996. Distribution of yttrium and rare-earth elements in the Penge and Kuruman iron-formations, Transvaal Supergroup, South Africa. Precambr. Res. 79, 37–55.

Baumgartner, L.K., Reid, R.P., Dupraz, C., Decho, A.W., Buckley, D.H., Spear, J.R., Przekop, K.M., Visscher, P.T., 2006. Sulfate reducing bacteria in microbial mats: Changing paradigms, new discoveries. Sed. Geol. 185, 131–145.

Beal, E.J., House, C.H., Orphan, V.J., 2009. Manganese- and iron-dependent marine methane oxidation. Science 325, 184–187.

Bekker, A., Slack, J.F., Planavsky, N., Krapež, B., Hofmann, A., Konhauser, K.O., Rouxel, O.J., 2010. Iron formation: The sedimentary product of a complex interplay among mantle, tectonic, oceanic, and biospheric processes. Econ. Geol. 105, 467–508.

Berner, R.A., 1989. Biogeochemical cycles of carbon and sulfur and their effect on atmospheric oxygen over phanerozoic time. Palaeogeogr. Palaeoclimatol. Palaeoecol. 75, 97–122.

Beukes, N., Swindell, E., Wabo, H., 2016. Manganese deposits of Africa. Episodes 39, 285–317.

Biondi, J.C., Lopez, M., 2017. Urucum Neoproterozoic-Cambrian manganese deposits (MS, Brazil): Biogenic participation in the ore genesis, geology, geochemistry, and depositional environment. Ore Geol. Rev. 91, 335–386.

Biondi, J.C., Polgári, M., Gyollai, I., Fintor, K., Kovács, I., Fekete, J., Mojzsis, S.J., 2020. Biogenesis of the Neoproterozoic kremydilite manganese ores from Urucum (Brazil) - a new manganese ore type. Precambr. Res. 340, 105624.

Brocks, J.J., Jarrett, A.J., Sirantoine, E., Hallmann, C., Hoshino, Y., Liyanage, T., 2017. The rise of algae in Cryogenian oceans and the emergence of animals. Nature 548, 578–581.

Brookins, D., 1988. Eh-pH Diagrams for Geochemistry. Springer-Verlag, Berlin, p. 176.

Cabral, A., Moore, J., Mapani, B., Koubová, M., Sattler, C.-D., 2011. Geochemical and mineralogical constraints on the genesis of the Otjosondu ferromanganese deposit, Namibia: hydrothermal exhalative versus hydrogenetic (including Snowball-Earth) origins. S. Afr. J. Geol. 114, 57–76.

Cai, C., Li, K., Liu, D., John, C., Wang, D., Fu, B., Fakhraee, M., He, H., Feng, L., Jiang, L., 2021. Anaerobic oxidation of methane by Mn oxides in sulfate-poor environments. Geology 49, 761–766.

Calvert, S., Pedersen, T., 1996. Sedimentary geochemistry of manganese: Implications for the environment of formation of manganiferous black shales. Econ. Geol. 91, 36–47.

Canfield, D.E., Farquhar, J., 2009. Animal evolution, bioturbation, and the sulfate concentration of the oceans. Proc. Natl. Acad. Sci. 106, 8123-8127.

Cavagna, S., Clari, P., Martire, L., 1999. The role of bacteria in the formation of cold seep carbonates: geological evidence from Monferrato (Tertiary, NW Italy). Sed. Geol. 126, 253–270.

Chen, F., Pufahl, P.K., Wang, Q., Matheson, E.J., Shabaga, B.M., Zhang, Q., Zeng, Y., Le, X., Ruan, D., Zhao, Y., 2022. A New Model for the Genesis of Carboniferous Mn Ores, Longtou Deposit, South China Block. Econ. Geol. 117, 107–125.

Cheng, M., Li, C., Chen, X., Zhou, L., Algeo, T.J., Ling, H.-F., Feng, L.-J., Jin, C.-S., 2018. Delayed Neoproterozoic oceanic oxygenation: evidence from Mo isotopes of the Cryogenian Datangpo Formation. Precambr. Res. 319, 187–197.

Cheng, M., Zhang, Z., Algeo, T.J., Liu, S., Liu, X., Wang, H., Chang, B., Jin, C., Pan, W., Cao, M., Li, C., 2021. Hydrological controls on marine chemistry in the Cryogenian Nanhua Basin (South China). Earth Sci. Rev. 218, 103678.

Clement, B.G., Luther, G.W., Tebo, B.M., 2009. Rapid, oxygen-dependent microbial Mn (II) oxidation kinetics at sub-micromolar oxygen concentrations in the Black Sea suboxic zone. Geochim. Cosmochim. Acta 73, 1878–1889.

Condie, K.C., Des Marais, D.J., Abbott, D., 2001. Precambrian superplumes and supercontinents: a record in black shales, carbon isotopes, and paleoclimates? Precambr. Res. 106, 239–260.

Condon, D., Zhu, M., Bowring, S., Wang, W., Yang, A., Jin, Y., 2005. U-Pb ages from the Neoproterozoic Doushantuo Formation, China. Science 308, 95–98.

Costerton, J.W., Lewandowski, Z., Caldwell, D.E., Korber, D.R., Lappin-Scott, H.M., 1995. Microbial biofilms. Annu. Rev. Microbiol. 49, 711–745.

De Putter, T., Liégeois, J.-P., Dewaele, S., Cailteux, J., Boyce, A., Mees, F., 2018. Paleoproterozoic manganese and base metals deposits at Kisenge-Kamata (Katanga, DR Congo). Ore Geol. Rev. 96, 181–200.

DeFarge, C., Trichet, J., Jaunet, A.-M., Robert, M., Tribble, J., Sansone, F.J., 1996. Texture of microbial sediments revealed by cryo-scanning electron microscopy. J. Sediment. Res. 66, 935–947.

Diem, D., Stumm, W., 1984. Is dissolved Mn^{2+} being oxidized by O_2 in absence of Mn-bacteria or surface catalysts? Geochim. Cosmochim. Acta 48, 1571–1573.

Dupraz, C., Reid, R.P., Braissant, O., Decho, A.W., Norman, R.S., Visscher, P.T., 2009. Processes of carbonate precipitation in modern microbial mats. Earth Sci. Rev. 96, 141–162.

Fan, D., Liu, T., Ye, J., 1992. The process of formation of manganese carbonate deposits hosted in black shale series. Econ. Geol. 87, 1419–1429.

Fan, D., Ye, J., Yin, L., Zhang, R., 1999. Microbial processes in the formation of the Sinian Gaoyan manganese carbonate ore, Sichuan Province, China. Ore Geol. Rev. 15, 79–93.

Friese, A., Bauer, K., Glombitza, C., Ordoñez, L., Ariztegui, D., Heuer, V.B., Vuillemin, A., Henny, C., Nomosatryo, S., Simister, R., Wagner, D., Bijaksana, S., Vogel, H., Melles, M., Russell, J.M., Crowe, S.A., Kallmeyer, J., 2021. Organic matter mineralization in modern and ancient ferruginous sediments. Nat. Commun. 12, 1–9.
Gao, Z., Zhu, X., Wang, D., Pan, C., Yan, B., Li, J., 2021. Insights into hydrothermal controls and processes leading to the formation of the Late Ediacaran Gaoyan stratiform manganese-carbonate deposit, Southwest China. Ore Geol. Rev. 139, 104524.
Guilbaud, R., Poulton, S.W., Thompson, J., Husband, K.F., Zhu, M., Zhou, Y., Shields, G. A., Lenton, T.M., 2020. Phosphorus-limited conditions in the early Neoproterozoic ocean maintained low levels of atmospheric oxygen. Nat. Geosci. 13, 296–301.
Gumsley, A.P., Chamberlain, K.R., Bleeker, W., Söderlund, U., de Kock, M.O., Larsson, E. R., Bekker, A., 2017. Timing and tempo of the Great Oxidation Event. Proc. Natl. Acad. Sci. U. S. A. 114, 1811–1816.
Häusler, K., Dellwig, O., Schnetger, B., Feldens, P., Leipe, T., Moros, M., Pollehne, F., Schönke, M., Wegwerth, A., Arz, H.W., 2018. Massive Mn carbonate formation in the Landsort Deep (Baltic Sea): hydrographic conditions, temporal succession, and Mn budget calculations. Mar. Geol. 395, 260–270.
Havig, J.R., McCormick, M.L., Hamilton, T.L., Kump, L.R., 2015. The behavior of biologically important trace elements across the oxic/euxinic transition of meromictic Fayetteville Green Lake, New York, USA. Geochim. Cosmochim. Acta 165, 389–406.
Heimann, A., Johnson, C.M., Beard, B.L., Valley, J.W., Roden, E.E., Spicuzza, M.J., Beukes, N.J., 2010. Fe, C, and O isotope compositions of banded iron formation carbonates demonstrate a major role for dissimilatory iron reduction in ~2.5 Ga marine environments. Earth Planet. Sci. Lett. 294, 8–18.
Henkel, J.V., Dellwig, O., Pollehne, F., Herlemann, D.P.R., Leipe, T., Schulz-Vogt, H.N., 2019. A bacterial isolate from the Black Sea oxidizes sulfide with manganese(IV) oxide. Proc. Natl. Acad. Sci. 116, 12153–12155.
Herndon, E.M., Havig, J.R., Singer, D.M., McCormick, M.L., Kump, L.R., 2018. Manganese and iron geochemistry in sediments underlying the redox-stratified Fayetteville Green Lake. Geochim. Cosmochim. Acta 231, 50–63.
Hoffman, P.F., Kaufman, A.J., Halverson, G.P., Schrag, D.P., 1998. A Neoproterozoic Snowball Earth. Science 281, 1342–1346.
Hoffman, P.F., Schrag, D.P., 2002. The Snowball Earth hypothesis: testing the limits of global change. Terra Nova 14, 129–155.
Hoffman, P.F., Abbot, D.S., Ashkenazy, Y., Benn, D.I., Brocks, J.J., Cohen, P.A., Cox, G. M., Creveling, J.R., Donnadieu, Y., Erwin, D.H., Fairchild, I.J., Ferreira, D., Goodman, J.C., Halverson, G.P., Jansen, M.F., Le Hir, G., Love, G.D., Macdonald, F. A., Maloof, A.C., Partin, C.A., Ramstein, G., Rose, B.E.J., Rose, C.V., Sadler, P.M., Tziperman, E., Voigt, A., Warren, S.G., 2017. Snowball Earth climate dynamics and Cryogenian geology-geobiology. Sci. Adv. 3, e1600983.
Hu, W., Kang, X., Cao, J., Wang, X., Fu, B., Wu, H., 2018. Thermochemical oxidation of methane induced by high-valence metal oxides in a sedimentary basin. Nat. Commun. 9, 1–11.
Huang, Q., Pi, D., Jiang, S., Liu, D., Yan, H., Mänd, K., Kirsimäe, K., Bishop, B., Robbins, L.J., Yang, S., 2022. The dual role of microbes in the formation of the Malkantu manganese carbonate deposit, NW China: Petrographic, geochemical, and experimental evidence. Chem. Geol. 606, 120992.
Huckriede, H., Meischner, D., 1996. Origin and environment of manganese-rich sediments within black-shale basins. Geochim. Cosmochim. Acta 60, 1399–1413.
Ivanets, A., Katsoshvili, L., Krivoshapkin, P., Prozorovich, V., Kuznetsova, T., Krivoshapkina, E., Radkevich, A., Zarubo, A., 2017. Sorption of strontium ions onto mesoporous manganese oxide of OMS-2 type. Radiochemistry 59, 264–271.
Jiang, G., Kennedy, M.J., Christie-Blick, N., Wu, H., Zhang, S., 2006. Stratigraphy, sedimentary structures, and textures of the Late Neoproterozoic Doushantuo cap carbonate in South China. J. Sediment. Res. 76, 978–995.
Jilbert, T., Slomp, C.P., 2013. Iron and manganese shuttles control the formation of authigenic phosphorus minerals in the euxinic basins of the Baltic Sea. Geochim. Cosmochim. Acta 107, 155–169.
Johnson, J.E., Webb, S.M., Ma, C., Fischer, W.W., 2016. Manganese mineralogy and diagenesis in the sedimentary rock record. Geochim. Cosmochim. Acta 173, 210–231.
Kasemann, S.A., Hawkesworth, C.J., Prave, A.R., Fallick, A.E., Pearson, P.N., 2005. Boron and calcium isotope composition in Neoproterozoic carbonate rocks from Namibia: evidence for extreme environmental change. Earth Planet. Sci. Lett. 231, 73–86.
Keil, R.G., 2011. Terrestrial influences on carbon burial at sea. Proc. Natl. Acad. Sci. U. S. A. 108, 9729–9730.
Klein, C., 2005. Some Precambrian banded iron-formations (BIFs) from around the world: Their age, geologic setting, mineralogy, metamorphism, geochemistry, and origin. Am. Mineral. 90, 1473–1499.
Klein, C., Ladeira, E.A., 2004. Geochemistry and mineralogy of Neoproterozoic banded iron-formations and some selected, siliceous manganese formations from the Urucum District, Mato Grosso do Sul, Brazil. Econ. Geol. 99, 1233–1244.
Konhauser, K.O., Hamade, T., Raiswell, R., Morris, R.C., Ferris, F.G., Southam, G., Canfield, D.E., 2002. Could bacteria have formed the Precambrian banded iron formations? Geology 30, 1079–1082.
Lau, K.V., Macdonald, F.A., Maher, K., Payne, J.L., 2017. Uranium isotope evidence for temporary ocean oxygenation in the aftermath of the Sturtian Snowball Earth. Earth Planet. Sci. Lett. 458, 282–292.
Learman, D.R., Wankel, S.D., Webb, S.M., Martinez, N., Madden, A.S., Hansel, C.M., 2011. Coupled biotic-abiotic Mn(II) oxidation pathway mediates the formation and structural evolution of biogenic Mn oxides. Geochim. Cosmochim. Acta 75, 6048–6063.
Li, Z.-X., Li, X., Kinny, P.D., Wang, J., 1999. The breakup of Rodinia: did it start with a mantle plume beneath South China? Earth Planet. Sci. Lett. 173, 171–181.
Li, C., Love, G.D., Lyons, T.W., Scott, C.T., Feng, L., Huang, J., Chang, H., Zhang, Q., Chu, X., 2012. Evidence for a redox stratified Cryogenian marine basin, Datangpo Formation, South China. Earth Planet. Sci. Lett. 331–332, 246–256.
Liu, X., Li, A., Dong, J., Zhuang, G., Xu, F., Wan, S., 2018. Nonevaporative origin for gypsum in mud sediments from the East China Sea shelf. Mar. Chem. 205, 90–97.
Maynard, J.B., 2010. The chemistry of manganese ores through time: a signal of increasing diversity of earth-surface environments. Econ. Geol. 105, 535–552.
Maynard, J.B., 2014. 9.11 - Manganiferous sediments, rocks, and ores. In: Holland, H.D., Turekian, K.K. (Eds.), Treatise on geochemistry (second edition). Elsevier, Oxford, pp. 327–349.
Morgan, J.J., 2005. Kinetics of reaction between O_2 and Mn (II) species in aqueous solutions. Geochim. Cosmochim. Acta 69, 35–48.
Mucci, A., 2004. The behavior of mixed Ca-Mn carbonates in water and seawater: Controls of manganese concentrations in marine porewaters. Aquat. Geochem. 10, 139–169.
Myers, C.R., Nealson, K.H., 1988. Bacterial manganese reduction and growth with manganese oxide as the sole electron acceptor. Science 240, 1319–1321.
Nealson, K.H., Saffarini, D., 1994. Iron and manganese in anaerobic respiration: Environmental significance, physiology, and regulation. Annu. Rev. Microbiol. 48, 311–343.
Ning, M., Yang, F., Ma, H., Lang, X., Shen, B., 2021. Precipitation of Marinoan cap carbonate from Mn-enriched seawater. Earth Sci. Rev. 218, 103666.
Ohnuki, T., Ozaki, T., Kozai, N., Nankawa, T., Sakamoto, F., Sakai, T., Suzuki, Y., Francis, A., 2008. Concurrent transformation of Ce (III) and formation of biogenic manganese oxides. Chem. Geol. 253, 23–29.
Okita, P.M., Maynard, J.B., Spiker, E.C., Force, E.R., 1988. Isotopic evidence for organic matter oxidation by manganese reduction in the formation of stratiform manganese carbonate ore. Geochim. Cosmochim. Acta 52, 2679–2685.
Okita, P.M., Shanks III, W.C., 1992. Origin of stratiform sediment-hosted manganese carbonate ore deposits: Examples from Molango, Mexico, and TaoJiang, China. Chem. Geol. 99, 139–163.
Planavsky, N.J., Asael, D., Hofmann, A., Reinhard, C.T., Lalonde, S.V., Knudsen, A., Wang, X., Ossa Ossa, F., Pecoits, E., Smith, A.J.B., Beukes, N.J., Bekker, A., Johnson, T.M., Konhauser, K.O., Lyons, T.W., Rouxel, O.J., 2014. Evidence for oxygenic photosynthesis half a billion years before the Great Oxidation Event. Nat. Geosci. 7, 283–286.
Polgári, M., Hein, J., Tóth, A., Pál-Molnár, E., Vigh, T., Bíró, L., Fintor, K., 2012a. Microbial action formed Jurassic Mn-carbonate ore deposit in only a few hundred years (Úrkút, Hungary). Geology 40, 903–906.
Polgári, M., Hein, J., Vigh, T., Szabó-Drubina, M., Fórizs, I., Bíró, L., Müller, A., Tóth, A., 2012b. Microbial processes and the origin of the Úrkút manganese deposit, Hungary. Ore Geol. Rev. 47, 87–109.
Polgári, M., Gyollai, I., Fintor, K., Horváth, H., Pál-Molnár, E., Biondi, J., 2019. Microbially mediated ore-forming processes and cell mineralization. Front. Microbiol. 10, 2731.
Polgári, M., Gyollai, I., 2021. Geochemical constraints on the element enrichments of microbially mediated manganese and iron ores - An overview. Ore Geol. Rev. 136, 104203.
Rajabzadeh, M.A., Haddad, F., Polgári, M., Fintor, K., Walter, H., Molnár, Z., Gyollai, I., 2017. Investigation on the role of microorganisms in manganese mineralization from Abadeh-Tashk area, Fars Province, southwestern Iran by using petrographic and geochemical data. Ore Geol. Rev. 80, 229–249.
Rodriguez-Navarro, C., Jimenez-Lopez, C., Rodriguez-Navarro, A., Gonzalez-Munoz, M. T., Rodriguez-Gallego, M., 2007. Bacterially mediated mineralization of vaterite. Geochim. Cosmochim. Acta 71, 1197–1213.
Rosson, R.A., Nealson, K.H., 1982. Manganese binding and oxidation by spores of a marine bacillus. J. Bacteriol. 151, 1027–1034.
Roy, S., 2006. Sedimentary manganese metallogenesis in response to the evolution of the Earth system. Earth Sci. Rev. 77, 273–305.
Sánchez-Román, M., Fernández-Remolar, D., Amils, R., Sánchez-Navas, A., Schmid, T., Martin-Uriz, P.S., Rodríguez, N., McKenzie, J.A., Vasconcelos, C., 2014. Microbial mediated formation of Fe-carbonate minerals under extreme acidic conditions. Sci. Rep. 4, 1–4.
Shields, G.A., 2005. Neoproterozoic cap carbonates: a critical appraisal of existing models and the plumeworld hypothesis. Terra Nova 17, 299–310.
Sholkovitz, E.R., Landing, W.M., Lewis, B.L., 1994. Ocean particle chemistry: the fractionation of rare earth elements between suspended particles and seawater. Geochim. Cosmochim. Acta 58, 1567–1579.
Siahi, M., Tsikos, H., Rafuza, S., Oonk, P.B.H., Mhlanga, X.R., van Niekerk, D., Mason, P. R.D., Harris, C., 2020. Insights into the processes and controls on the absolute abundance and distribution of manganese in Precambrian iron formations. Precambr. Res. 350, 105878.
Smith, A.J.B., 2015. RESEARCH FOCUS: The life and times of banded iron formations. Geology 43, 1111–1112.
Smith, A.J.B., Beukes, N.J., Gutzmer, J., 2013. The Composition and Depositional Environments of Mesoarchean Iron Formations of the West Rand Group of the Witwatersrand Supergroup, South Africa. Econ. Geol. 108, 111–134.
Smith, A.J.B., Beukes, N.J., 2023. The paleoenvironmental implications of pre-Great Oxidation Event manganese deposition in the Mesoarchean Ijzermijn Iron Formation Bed, Mozaan Group, Pongola Supergroup, South Africa. Precambr. Res. 384, 106922.
Smith, A.J.B., Beukes, N.J., Cochrane, J.M., Gutzmer, J., 2023. Manganese carbonate-bearing mudstone of the Witwatersrand-Mozaan succession in southern Africa as

evidence for bacterial manganese respiration and availability of free molecular oxygen in Mesoarchaean oceans. S. Afr. J. Geol. 126, 29–48.
Stumm, W., Morgan, J., 1995. Aquatic Chemistry: Chemical Equilibria and Rates in Natural Waters (3rd Edition). John Wiley, New York, p. 1040.
Suess, E., 1979. Mineral phases formed in anoxic sediments by microbial decomposition of organic matter. Geochim. Cosmochim. Acta 43, 339–352.
Sutherland, K.M., Wankel, S.D., Hansel, C.M., 2018. Oxygen isotope analysis of bacterial and fungal manganese oxidation. Geobiology 16, 399–411.
Taillefert, M., Gaillard, J.F., 2002. Reactive transport modeling of trace elements in the water column of a stratified lake: iron cycling and metal scavenging. J. Hydrol. 256, 16–34.
Tanaka, K., Tani, Y., Takahashi, Y., Tanimizu, M., Suzuki, Y., Kozai, N., Ohnuki, T., 2010. A specific Ce oxidation process during sorption of rare earth elements on biogenic Mn oxide produced by Acremonium sp. strain KR21-2. Geochim. Cosmochim. Acta 74, 5463–5477.
Tebo, B.M., Ghiorse, W.C., van Waasbergen, L.G., Siering, P.L., Caspi, R., 1997. Bacterially mediated mineral formation: Insights into manganese (II) oxidation from molecular genetic and biochemical studies. Rev. Mineral. Geochem. 35, 225–266.
Taylor, S.R., McLennan, S.M., 1985. The continental crust: its composition and evolution. Blackwell Scientific, Oxford, p. 312.
Tebo, B.M., Bargar, J.R., Clement, B.G., Dick, G.J., Murray, K.J., Parker, D., Verity, R., Webb, S.M., 2004. Biogenic manganese oxides: properties and mechanisms of formation. Annu. Rev. Earth Planet. Sci. 32, 287–328.
Thamdrup, B., Rosselló-Mora, R., Amann, R., 2000. Microbial manganese and sulfate reduction in Black Sea shelf sediments. Appl. Environ. Microbiol. 66, 2888–2897.
Thompson, J.B., Schultze-Lam, S., Schultze-Lam, S., Beveridge, T.J., Des Marais, D.J., 1997. Whiting events: Biogenic origin due to the photosynthetic activity of cyanobacterial picoplankton. Limnol. Oceanogr. 42, 133–141.
Van Cappellen, P., Viollier, E., Roychoudhury, A., Clark, L., Ingall, E., Lowe, K., Dichristina, T., 1998. Biogeochemical cycles of manganese and iron at the oxic–anoxic transition of a stratified marine basin (Orca Basin, Gulf of Mexico). Environ. Sci. Tech. 32, 2931–2939.
Veizer, J., Hoefs, J., Ridler, R., Jensen, L., Lowe, D., 1989. Geochemistry of Precambrian carbonates: I. Archean hydrothermal systems. Geochim. Cosmochim. Acta 53, 845–857.
Vickerman, J.C., Briggs, D., 2013. ToF-SIMS: Materials Analysis by Mass Spectrometry, Second Edition. IM Publications and SurfaceSpectra.
Wang, T.G., 2022. Meso-Neoproterozoic Geology and Petroleum Resources in China. Springer Nature, p. 179.
Wang, P., Du, Y., Yu, W., Algeo, T.J., Zhou, Q., Xu, Y., Qi, L., Yuan, L., Pan, W., 2020. The chemical index of alteration (CIA) as a proxy for climate change during glacial-interglacial transitions in Earth history. Earth Sci. Rev. 201, 103032.
Wang, J., Li, Z.-X., 2003. History of Neoproterozoic rift basins in South China: implications for Rodinia break-up. Precambr. Res. 122, 141–158.
Wang, C., Shi, G., 2019. Redox condition and organic carbon accumulation mechanism in the Cryogenian Nanhua Basin, South China: Insights from iron chemistry and sulfur, carbon, oxygen isotopes of the Datangpo Formation. Adv. Geo-Energy Res. 3, 67–75.
Webb, S.M., Dick, G.J., Bargar, J.R., Tebo, B.M., 2005. Evidence for the presence of Mn (III) intermediates in the bacterial oxidation of Mn (II). Proc. Natl. Acad. Sci. U. S. A. 102, 5558–5563.
Whiticar, M.J., 1999. Carbon and hydrogen isotope systematics of bacterial formation and oxidation of methane. Chem. Geol. 161, 291–314.
Wittkop, C., Swanner, E., Grengs, A., Lambrecht, N., Fakhraee, M., Myrbo, A., Bray, A., Poulton, S., Katsev, S., 2020. Evaluating a primary carbonate pathway for manganese enrichments in reducing environments. Earth Planet. Sci. Lett. 538, 116201.
Wu, C., Zhang, Z., Xiao, J., Fu, Y., Shao, S., Zheng, C., Yao, J., Xiao, C., 2016. Nanhuan manganese deposits within restricted basins of the southeastern Yangtze Platform, China: Constraints from geological and geochemical evidence. Ore Geol. Rev. 75, 76–99.
Xiao, J., He, J., Yang, H., Wu, C., 2017. Comparison between Datangpo-type manganese ores and modern marine ferromanganese oxyhydroxide precipitates based on rare earth elements. Ore Geol. Rev. 89, 290–308.
Ye, Y., Wang, H., Zhai, L., Wang, X., Wu, C., Zhang, S., 2018. Contrasting Mo-U enrichments of the basal Datangpo Formation in South China: Implications for the Cryogenian interglacial ocean redox. Precambr. Res. 315, 66–74.
Yu, W., Algeo, T.J., Du, Y., Maynard, B., Guo, H., Zhou, Q., Peng, T., Wang, P., Yuan, L., 2016. Genesis of Cryogenian Datangpo manganese deposit: Hydrothermal influence and episodic post-glacial ventilation of Nanhua Basin, South China. Palaeogeogr. Palaeoclimatol. Palaeoecol. 459, 321–337.
Yu, W., Algeo, T.J., Du, Y., Zhou, Q., Wang, P., Xu, Y., Yuan, L., Pan, W., 2017. Newly discovered Sturtian cap carbonate in the Nanhua Basin, South China. Precambr. Res. 293, 112–130.
Yu, W., Polgári, M., Gyollai, I., Fintor, K., Szabó, M., Kovács, I., Fekete, J., Du, Y., Zhou, Q., 2019. Microbial metallogenesis of Cryogenian manganese ore deposits in South China. Precambr. Res. 322, 122–135.
Yu, W., Algeo, T.J., Zhou, Q., Du, Y., Wang, P., 2020. Cryogenian cap carbonate models: a review and critical assessment. Palaeogeogr. Palaeoclimatol. Palaeoecol. 552, 109727.
Yu, W., Polgári, M., Gyollai, I., Fintor, K., Huang, H., Szabó, M., Du, Y., 2021. Microbial metallogenesis of early carboniferous manganese deposit in central Guangxi, South China. Ore Geol. Rev. 136, 104251.
Yu, W., Algeo, T.J., Zhou, Q., Wei, W., Yang, M., Li, F., Du, Y., Pan, W., Wang, P., 2022. Evaluation of alkalinity sources to Cryogenian cap carbonates, and implications for cap carbonate formation models. Global Planet. Change 217, 103949.
Zhang, B., Cao, J., Liao, Z., Zhang, Y., Wu, Q., Shi, C., Hu, K., 2021. Dynamic biogeochemical cycling and mineralization of manganese of hydrothermal origin after the Marinoan glaciation. Chem. Geol. 584, 120502.
Zhang, S., Jiang, G., Zhang, J., Song, B., Kennedy, M.J., Christie-Blick, N., 2005. U-Pb sensitive high-resolution ion microprobe ages from the Doushantuo Formation in South China: Constraints on late Neoproterozoic glaciations. Geology 33, 473–476.
Zhang, S., Jiang, G., Han, Y., 2008. The age of the Nantuo Formation and Nantuo glaciation in South China. Terra Nova 20, 289–294.
Zhang, H., Li, Y., Wang, X., Lu, A., Ding, H., Zeng, C., Wang, X., Wu, X., Nie, Y., Wang, C., 2015b. Aerobic and anaerobic reduction of birnessite by a novel Dietzia strain. Geochem. Trans. 16, 11.
Zhang, F., Zhu, X., Yan, B., Kendall, B., Peng, X., Li, J., Algeo, T.J., Romaniello, S., 2015a. Oxygenation of a Cryogenian ocean (Nanhua Basin, South China) revealed by pyrite Fe isotope compositions. Earth Planet. Sci. Lett. 429, 11–19.
Zhao, L., Cai, C., Jin, R., Li, J., Li, H., Wei, J., Guo, H., Zhang, B., 2018. Mineralogical and geochemical evidence for biogenic and petroleum-related uranium mineralization in the Qianjiadian deposit, NE China. Ore Geol. Rev. 101, 273–292.
Zhou, Q., Du, Y., Qin, Y., 2013. Ancient natural gas seepage sedimentary-type manganese metallogenic system and ore-forming model: A case study of Datangpo type manganese deposits formed in rift basin of Nanhua period along Guizhou-Hunan-Chongqing border area. Miner. Depos. 32, 457–466.
Zhou, Q., Du, Y., Yuan, L., Zhang, S., Yu, W., Yang, S., Liu, Y., 2016. Rift basin structure and its control function in Nanhua Period of Guizhou-Hunan-Chongqing Border Area. Earth Sci. (J. China Univ. Geosci.-Wuhan) 41, 177–188.
Zhou, C., Tucker, R., Xiao, S., Peng, Z., Yuan, X., Chen, Z., 2004. New constraints on the ages of Neoproterozoic glaciations in South China. Geology 32, 437–440.